On spatial variations of the electron-to-proton mass ratio in the Milky Way

S. A. Levshakov[1], P. Molaro[2], and M. G. Kozlov[3]
[1]*Ioffe Physico-Technical Institute, Politekhnicheskaya Str. 26, 194021 St. Petersburg, Russia*
[2]*INAF-Osservatorio Astronomico di Trieste, Via G. B. Tiepolo 11, 34131 I, Trieste, Italy and*
[3]*Petersburg Nuclear Physics Institute, Gatchina, 188300, Russia*
(Dated: August 5, 2008)

We aim at applying the ammonia method, recently proposed to explore the electron-to-proton mass ratio $\mu = m_{\rm e}/m_{\rm p}$, to Galactic sources. Emission lines due to ammonia are originated in the numerous interstellar molecular clouds allowing to probe μ at different galactocentric distances. High quality radio-astronomical observations of molecular cores in lines of NH_3 $(J,K) = (1,1)$, CCS $J_N = 2_1 - 1_0$, HC_3N $J = 5-4$, and N_2H^+ $J = 1-0$ are used to measure the relative radial velocity offsets, ΔV, between the NH_3 (1,1) and other molecular transitions. Robust statistical analysis is applied to the $n = 207$ individual measurements in the Perseus molecular cloud (PC), the Pipe Nebula (PN), and the infrared dark clouds (IRDCs) to deduce the mean value of ΔV and its uncertainty. The measured values of ΔV from the PC, PN, and IRDCs show statistically significant positive velocity shifts between the line centers of NH_3 and other molecules. The most accurate estimates are obtained from carefully selected subsamples of the NH_3/CCS pairs observed in the PC ($n = 21$) and the PN ($n = 8$), $\Delta V = 36 \pm 7_{\rm stat} \pm 13.5_{\rm sys}$ m s^{-1} and $53 \pm 11_{\rm stat} \pm 13.5_{\rm sys}$ m s^{-1}, respectively, and from the $n = 36$ NH_3/N_2H^+ and $n = 27$ NH_3/HC_3N pairs observed in the IRDCs, $\Delta V = 148 \pm 32_{\rm stat} \pm 13.6_{\rm sys}$ m s^{-1} and $115 \pm 37_{\rm stat} \pm 31_{\rm sys}$ m s^{-1}, respectively. Being interpreted in terms of the electron-to-proton mass ratio variation, this gives $\Delta\mu/\mu \sim (4-14)\times 10^{-8}$, which is an order of magnitude more sensitive than previous astronomical constraints on this quantity. If $\Delta\mu/\mu$ follows the gradient of the local gravitational potential, as suggested in some scalar field models, then the obtained result is in sharp contradiction (~ 5 orders of magnitude) with laboratory atomic clock experiments carried out at different points in the gravitational potential of the Sun. However, the measured signal might be consistent with chameleon-type scalar field models which predict a strong dependence of masses and coupling constants on the ambient matter density. The confirmation of a spatial variation of $\Delta\mu/\mu$ will help to distinguish between many theoretical proposals suggested to explain the nature of dark energy. New control measurements of the velocity offsets involving other molecules and a wider range of objects along with verification of rest frequencies are needed to investigate different instrument systematics and to come to a more certain conclusion.

PACS numbers: 06.20.Jr, 32.30.Bv, 95.36+x, 95.85.Bh, 98.38.Bn, 98.38.Dq

I. INTRODUCTION

A fundamental characteristic of the universe is that decelerating expansion changed to accelerating at redshift $z \sim 1$ [1, 2, 3]. This late time acceleration is usually attributed to some negative-pressure component of the bulk of energy density, referred to as 'dark energy'. The nature of dark energy remains unknown in spite of a good deal of theoretical and experimental efforts [4]. The most popular scenario is a dynamically evolving scalar field φ, named 'quintessence' [5], with the energy density subdominant at a matter dominated (decelerating) epoch ($1 \lesssim z \lesssim 1000$), and dominant at lower redshifts [6]. Scalar field models allow to alleviate the so-called 'cosmic coincidence' problem – the fact that matter and vacuum energy contribute by comparable amounts to the energy density at the present cosmological epoch [7]. The scalar field(s) coupling to ordinary matter leads unavoidably to long-range forces and variability of the physical constants violating the Equivalence Principle. Thus, any laboratory or space-based experiments as well as astronomical studies aimed at probing the variations of the physical constants, are the most important tools to test new theories against observations.

Present experimental facilities allow us to probe the variability of the fine-structure constant $\alpha = e^2/(\hbar c)$ and the electron-to-proton mass ratio $\mu = m_{\rm e}/m_{\rm p}$, or different combinations of the proton gyromagnetic ratio $g_{\rm p}$ with α and μ [8].

The most accurate laboratory constraint on the temporal variation of α of $\dot\alpha/\alpha = (-1.6\pm2.3)\times10^{-17}$ yr^{-1} is obtained from atomic clocks experiments [9]. Being linearly extrapolated to redshift $z \sim 2$, or $t \sim 10^{10}$ yr, this laboratory bound leads to $\Delta\alpha/\alpha = (-1.6\pm2.3)\times10^{-7}$ which is well below a conservative upper limit on $|\Delta\alpha/\alpha| < 10^{-5}$ stemmed from the analysis of quasar absorption-line systems [10, 11, 12]. Here $\Delta\alpha/\alpha = (\alpha' - \alpha)/\alpha$, with α, α' denoting the values of the fine-structure constant in the laboratory and the specific absorption/emission line system of a galactic or extragalactic object (the same definition is applied to $\Delta\mu/\mu$). However, laboratory experiments and quasar absorption spectra investigate very different time scales and different regions of the universe, and the connection between them is somewhat model dependent [13, 14].

The direct and model-free estimate of time variation of μ was deduced from comparison of the frequency of a rovibrational transition in SF_6 molecule with the fundamental hyperfine transition in Cs: $\dot\mu/\mu = (3.8 \pm 5.6) \times$

10^{-14} yr^{-1} [15]. Astrophysical estimates of μ at high redshifs are controversial in the claims of nonzero and zero changes of μ: $\Delta\mu/\mu = (-2.4 \pm 0.6) \times 10^{-5}$ was inferred from the analysis of the H_2-bearing clouds at $z = 2.6$ and 3.0 [16], but this value was not confirmed later [17, 18]. A better accuracy bound was obtained at lower redshift $z = 0.68$ from the analysis of radio-frequency transitions in NH_3, CO, HCO^+, and HCN: $\Delta\mu/\mu = (-0.6 \pm 1.9) \times 10^{-6}$ [19], which favors a non-variability of μ at the level of $\sim 3 \times 10^{-6}$.

In these studies it was assumed that the rate of time variations dominates over the rate of possible spatial variations. However, this may not be the case if scalar fields trace the gravitational field inhomogeneities [20, 21]. The spatial variation of constants in a changing gravitational potential of the Sun were studied in laboratory measurements of the atomic clock transition $^1S_0$–$^3P_0$ in neutral ^{87}Sr relative to the Cs standard and of the radio-frequency $E1$ transition between nearly degenerate, opposite-parity levels of atomic dysprosium (Dy). The values for the couplings of α and μ to the gravitational field were reported to be $k_\alpha = (2.3 \pm 3.1) \times 10^{-6}$, $k_\mu = (-1.1 \pm 1.7) \times 10^{-5}$ [22], and $k_\alpha = (-8.7 \pm 6.6) \times 10^{-6}$ [23], respectively.

Thus, the current laboratory and astrophysical estimates of the temporal and/or spatial changes of the coupling constants and fermion masses do not exhibit any meaningful features which could be interpreted in terms of scalar field effects. On the other hand, we do observe the late time acceleration of the universe driven most probably by ultra-light scalar fields. To reconcile these results chameleon-type models were suggested [24, 25, 26, 27, 28, 29, 30] which allow scalar fields to evolve on cosmological time scales today and to have simultaneous strong couplings of order unity to matter, as expected from string theory. The key assumption in this scenario is that the mass of the scalar field depends on the local matter density. This explains why cosmological scalar fields, such as quintessence, are not detectable in local tests of the Equivalence Principle since we live in a dense environment where the mass of the field can be sufficiently large and φ-mediated interactions are short-ranged. On the other hand, the cosmological matter density is about 10^{30} times smaller and thus the mass of the scalar field can be very low, of order of H_0, the present Hubble constant. This allows the field to evolve cosmologically today. Laboratory experiments aimed at detections of chameleon particles are nowadays carried out at Fermilab [31].

In this paper we explore the astrophysical implications of the scalar field effect on the electron-to-proton mass ratio, μ, following suggestions on experimental tests of $\Delta\mu/\mu$ in our Galaxy as formulated in [30]. We consider the constraints on the spatial variations $\Delta\mu/\mu$ caused by the relative Doppler shifts of molecular transitions in cold molecular cores observed in the Milky Way disk at different galactocentric distances.

Our assumptions and basic physical properties of dense molecular cores which will be needed in the sequel are discussed in Sect. II. The statistical analysis of the line position measurements in the Perseus molecular complex, the Pipe Nebula, and the infrared dark clouds are presented in Sect. III. The obtained results are discussed in Sect. IV, and conclusions are given in Sect. V.

TABLE I: Molecular transitions and $V_{\rm LSR}$ uncertainties, ε_v, used in calculations of $\Delta\mu/\mu$. The numbers in parentheses correspond to 1σ errors (see Sect. IV A for more details).

Transition	$\nu_{\rm rest}$, GHz	$\lambda_{\rm rest}$, cm	ε_v, m s^{-1}
CCS $J_N = 2_1 - 1_0$	22.344033(1)[a]	1.34	13.4
NH_3 $(J,K) = (1,1)$	23.6944955(1)[a]	1.27	1.3
HC_3N $J = 5 - 4$	45.4903102(3)[b]	0.66	2.8
N_2H^+ $J = 1 - 0$	93.173777(4)[b]	0.32	13.5

[a] Rest frequency from Ref. 34.
[b] Rest frequency from Ref. 36.

II. INTERSTELLAR MOLECULES AS PROBES OF $\Delta\mu/\mu$ SPATIAL VARIATIONS

Extremely narrow molecular lines observed in cold dark clouds provide a sensitive spectroscopic tool to study the spatial variations of fundamental constants under different environments and gravitational fields. Among numerous molecules detected in the interstellar medium (ISM), ammonia (NH_3) is of particular interest due to its high sensitivity to changes in the electron-to-proton mass ratio, μ. As was firstly shown for ammonia isotopomer $^{15}ND_3$ [32], the inversion frequency in the $(J,K) = (1,1)$ level changes as

$$\frac{\Delta\nu}{\nu} = 5.6\frac{\Delta\mu}{\mu} , \qquad (1)$$

which is nearly an order of magnitude more sensitive to μ-variation than molecular vibrational frequencies which scale as $E_{\rm vib} \sim \mu^{1/2}$.

The deuterated ammonia shows, however, low abundances in the ISM molecular clouds, $n(ND_3)/n(NH_3) \simeq 10^{-4} - 10^{-2}$ [33]. For more abundant ammonia form of NH_3, the sensitivity coefficient of the inversion transition $\nu = 23.69$ GHz was calculated in [19]:

$$\frac{\Delta\nu}{\nu} = 4.46\frac{\Delta\mu}{\mu} . \qquad (2)$$

By comparing the observed inversion frequency of NH_3 (1,1) with a suitable rotational frequency (scaling as $E_{\rm rot} \sim \mu$) of another molecule arising *co-spatially* with ammonia, a limit on the spatial variation of μ can be determined [19]:

$$\frac{\Delta\mu}{\mu} = 0.289\frac{V_{\rm rot} - V_{\rm inv}}{c} \equiv 0.289\frac{\Delta V}{c} , \qquad (3)$$

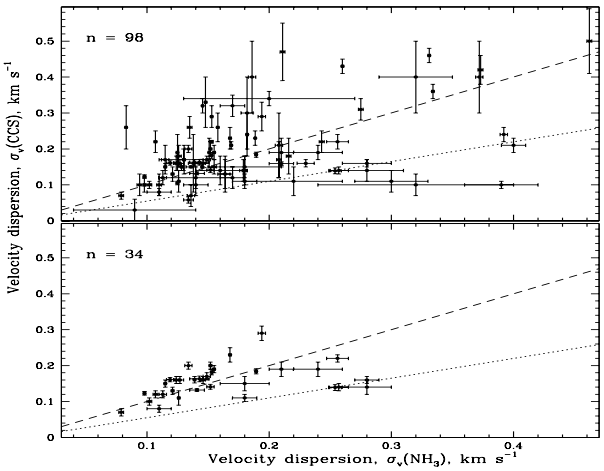

FIG. 1: *Upper panel*: CCS ($2_1 - 1_0$) versus $NH_3(1,1)$ linewidths for cores in the Perseus molecular cloud from the total sample of Ref. [34]. The error bars represent 1σ standard deviations. *Lower panel*: Subsample of the best quality single-component profiles of CCS and NH_3 selected from the full set of the observed spectra available online (see Table II). In both panels, the dashed and dotted lines are the boundaries for, respectively, pure turbulent, $\sigma_v(\mathrm{CCS}) = \sigma_v(\mathrm{NH_3})$, and pure thermal, $\sigma_v(\mathrm{CCS}) = 0.55\sigma_v(\mathrm{NH_3})$, line broadening. The sample sizes are indicated in the panels.

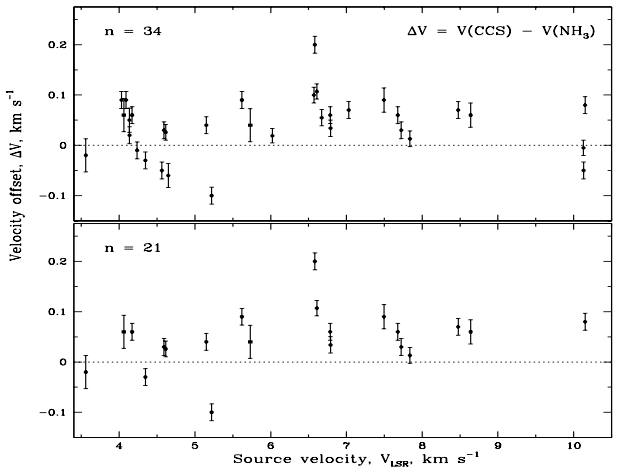

FIG. 2: *Upper panel*: Velocity offset $\Delta V_{\mathrm{CCS-NH_3}}$ versus the source radial velocity for points shown in Fig. 1, lower panel. *Lower panel*: Same as the upper panel but for the points marked by asterisks in Table II. The vertical error bars include both random and systematic errors caused by the uncertainties of the adopted rest frequencies (see Table I).

where V_{rot} and V_{inv} are the apparent radial velocities of the rotational and inversion transitions, respectively.

In the present paper we use the comparison of the relative radial velocities of ammonia inversion lines and rotational transitions of another N-bearing (N_2H^+) and C-bearing (CCS, HC_3N) molecules (Table I) to set a limit on spatial variations of $\Delta\mu/\mu$. Here we consider some physical and kinematic properties of the molecular gas clouds where these molecules are detected.

NH_3, N_2H^+, CCS, and HC_3N are usually observed in emission in dense molecular clouds ($n_{\mathrm{H}} \gtrsim 10^4$ cm^{-3}) which are represented by a large variety of types in the Milky Way disk [38]. Two main classes are high-mass clumps ($\mathcal{M} \gtrsim 100\mathcal{M}_\odot$) associated with infrared dark clouds (IRDCs), and low-mass cores ($\mathcal{M} \lesssim 10\mathcal{M}_\odot$) subdivided in turn into protostellar cores containing infrared sources, and starless cores (pre-protostellar, or prestellar cores) without embedded luminous sources of any mass. The latter provide information on the physical conditions of dense molecular gas preceding gravitational collapse. Depending on the critical gas density in the core center ($n_{\mathrm{H_2}} \sim 10^5$ cm^{-3}), the starless cores can be either dynamically stable against gravitational contraction ($n_{\mathrm{H_2}} \lesssim 10^5$ cm^{-3}), or unstable if density exceeds this critical value [39]. The dense cores reside within a larger molecular complex or can be isolated. With increasing angular resolution the cores reveal a substructure with its own range of masses. Being very sensitive to the environmental physical conditions, different molecules probe, in general, different substructures within the clouds.

At high spectral resolution available in the microwave range the errors in the molecular line position measurements are mainly restricted by the uncertainties in laboratory frequencies, $\varepsilon_\nu \sim 0.1-1$ kHz, which correspond to the V_{LSR} uncertainties of $\varepsilon_v \sim 1-10$ m s^{-1} [34]. Taking into account that $\Delta\mu/\mu \sim 0.3\Delta V/c$, the expected precision of the $\Delta\mu/\mu$ measurements in the ISM is restricted by the level of $\sim 10^{-8}$, i.e. they are about 100 times more accurate than the $\Delta\mu/\mu$ estimate deduced at $z = 0.68$ [19].

This level of accuracy can be achieved, however, only ideally since it assumes that molecules are identically (cospatially) distributed within the cloud, and are observed simultaneously with the same receiver, beam size, system temperature, and velocity resolution. Violation of any of these conditions leads to shifts of the line centers which are referred to as the *Doppler noise*. The input of the Doppler noise to a putative $\Delta\mu/\mu$ signal can be reduced to some extent if the velocity shifts due to inhomogeneous distribution of molecules and to instrumental imperfections are of random nature.

All molecular transitions listed in Table I require for their excitation high gas density, $n_{\mathrm{H}} \sim 10^4$ cm^{-3}, at a typical kinetic temperature of $T_{\mathrm{kin}} \sim 10$ K. Ammonia is easily detectable in many interstellar clouds. The inversion transition $(J, K) = (1, 1)$ has 18 hyperfine components which can be resolved into nine separate features for quiescent nearby dark clouds [40]. Since hyperfine components have different intensities, a single NH_3 spectrum allows to determine optical depth, radial velocity, intrinsic linewidth, and excitation temperature and thus to separate the effects of optical depth and excitation temperature [41].

The second N-bearing molecule, which is a good tracer of cold and quiescent dense gas, is the molecular ion N_2H^+. The seven hyperfine components of the N_2H^+

TABLE II: Parameters of dense cores in the Perseus molecular cloud ($D \simeq 260$ pc) taken from Ref. [34] and representing the best quality single component profiles of CCS ($2_1 - 1_0$) and NH_3 (1,1). Asterisk marks objects with $0.55\sigma_v(NH_3) \lesssim \sigma_v(CCS) \lesssim \sigma_v(NH_3)$ (see Fig. 1).

NH3SRC source	Other name	V_{LSR} (km s^{-1})	$\sigma_v(NH_3)$ (km s^{-1})	$\sigma_v(CCS)$ (km s^{-1})	ΔV_{CCS-NH_3} (km s^{-1})
3	B16	4.136(1)	0.115(1)	0.15(1)	0.02(1)
6	B11	4.030(3)	0.134(3)	0.20(1)	0.09(1)
7	B30	4.135(1)	0.168(1)	0.23(2)	0.05(2)
8	S57	4.090(1)	0.155(1)	0.19(1)	0.09(1)
9	B13	4.563(2)	0.124(2)	0.16(1)	−0.05(1)
11	B6	4.236(8)	0.143(8)	0.163(8)	−0.01(1)
13∗	B1	4.06(1)	0.24(2)	0.19(1)	0.06(2)
15	B27	4.648(3)	0.194(3)	0.29(2)	−0.06(2)
16∗	B4	4.614(7)	0.141(6)	0.132(4)	0.026(8)
19∗	B22	4.345(7)	0.256(9)	0.22(1)	−0.03(1)
20∗	B21	4.17(1)	0.28(1)	0.16(1)	0.06(1)
21∗	B20	3.559(9)	0.21(1)	0.19(2)	−0.02(3)
22∗	B10	5.150(2)	0.146(2)	0.16(1)	0.04(1)
24∗	B9	4.591(3)	0.149(3)	0.17(1)	0.03(1)
28∗	D7	5.62(1)	0.11(1)	0.08(1)	0.09(1)
30∗	L24	5.22(1)	0.18(1)	0.11(1)	−0.10(1)
46	B45	7.030(1)	0.152(1)	0.20(1)	0.07(1)
60∗	D4	5.73(2)	0.18(2)	0.15(2)	0.04(3)
87∗	B85	7.495(1)	0.126(1)	0.11(2)	0.09(2)
93	B18	6.022(1)	0.098(1)	0.123(5)	0.019(5)
96∗	B34	7.838(3)	0.152(3)	0.141(7)	0.013(8)
97∗	B32	7.724(2)	0.102(2)	0.10(1)	0.03(1)
111	B40	6.673(1)	0.139(1)	0.161(9)	0.055(9)
112∗	B75	6.583(7)	0.257(8)	0.14(1)	0.20(1)
113	B41	6.570(1)	0.153(1)	0.182(8)	0.100(8)
114∗	B42	6.609(1)	0.1894(9)	0.184(7)	0.107(7)
124∗	B44	6.786(1)	0.121(1)	0.13(1)	0.06(1)
126∗	B48	6.790(4)	0.254(5)	0.139(8)	0.034(9)
128∗	B58	7.678(2)	0.079(2)	0.07(1)	0.06(1)
142∗	B91	8.475(3)	0.113(3)	0.12(1)	0.07(1)
151∗	BS9	8.64(1)	0.28(2)	0.14(2)	0.06(2)
188∗	B121	10.151(2)	0.107(2)	0.12(1)	0.08(1)
190	L44	10.130(3)	0.119(3)	0.161(6)	−0.005(7)
191	D28	10.131(3)	0.127(3)	0.16(1)	−0.05(1)

$J = 1-0$ transition were studied with high spectral resolution in [42]. N_2H^+ is mainly formed in well-shielded regions where photoprocesses are unimportant [43]. The intensity distribution of N_2H^+ $(1-0)$ in dense cores closely matches that of NH_3 (1,1), and the relative abundances of these molecules are almost constant across the starless core. However, in some cases there were detections of ammonia abundances increased by a factor of ∼1-10 towards the core center [44]. High angular resolution observations of nearby prestellar objects show that N-bearing molecules trace the inner cores where the density approaches 10^5 cm^{-3} and the carbon-chain molecules disappear from the gas-phase because of the freeze-out onto dust grains [38]. The observed correlation between N_2H^+ and NH_3 velocities and linewidths is another indication of probable co-spatial origin of these two species [45].

The spectral lines of the radical CCS without hyperfine splittings and not strongly saturated ($\tau < 3$) make CCS a well-suited molecule for detailed studies of the velocity structure in dark clouds [46]. CCS lines are rather intense in starless, cold and quiescent dark clouds at the earliest stages of molecular cloud evolution, whereas NH_3, as mentioned above, tends to be abundant in more chemically evolved and dense central regions of molecular cores [47]. As a rule, CCS shows up as a clumpy distributed gas slightly outside these central regions. A pronounced spatial *anticorrelation* in the emission from CCS and NH_3 was observed on large scale maps of the Taurus Molecular Cloud 1 (TMC-1) ridge [48], pre-protostellar cores L1498 [49] and B68 [50], as well as on small scale maps with angular resolution of $\simeq 5''$ (= 1750 AU) in the infrared cloud B1-IRS where the CCS emission was detected from three clumps surrounding the central source [51]. The clumps in B1-IRS exhibit a velocity gradient from red- to blueshifted velocities with respect to the systemic velocity of the central source which can be interpreted as interaction of the CCS-emitting gas with the molecular outflow. This interaction makes CCS lines wider than their thermal widths and comparable with the measured widths of the NH_3 lines in the B1-IRS source: $\sigma_v(CCS) = 0.9 \pm 0.1$ km s^{-1} and $\sigma_v(NH_3) = 1.1 \pm 0.1$ km s^{-1} (CCS thermal linewidth is narrower by a factor of 0.55 than that of NH_3 due to the different masses of these molecules). Turbulent broadening could equalize the apparent linewidths if both CCS and NH_3 trace the

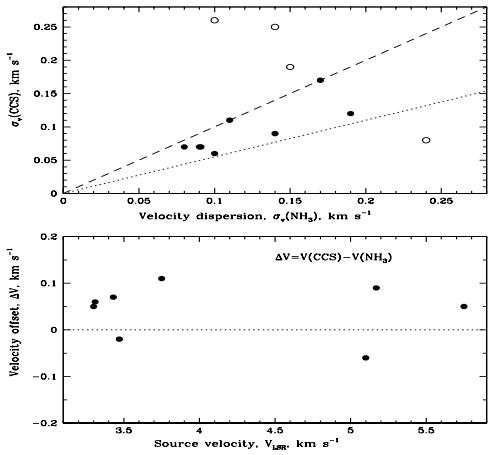

FIG. 3: *Upper panel*: CCS ($2_1 - 1_0$) versus NH_3(1,1) linewidths for dense cores associated with the Pipe Nebulae from the survey of Ref. [65]. No error bars were reported in the original paper. The filled circles represent points marked by asterisks in Table III. The dashed and dotted lines are the boundaries for, respectively, pure turbulent, $\sigma_v(\mathrm{CCS}) = \sigma_v(\mathrm{NH_3})$, and pure thermal, $\sigma_v(\mathrm{CCS}) = 0.55\sigma_v(\mathrm{NH_3})$, line broadening. *Lower panel*: Velocity offset $\Delta V_{\mathrm{CCS-NH_3}}$ versus the source radial velocity set by $V_{\mathrm{LSR}}(\mathrm{NH_3})$.

TABLE III: Parameters of dense cores in the Pipe Nebula ($D \simeq 130$ pc) taken from Ref. [65] and representing emission line profiles of CCS ($2_1 - 1_0$) and NH_3 (1,1). Asterisk marks filled circles in Fig. 3.

Source	V_{LSR}, km s^{-1}		σ_v, km s^{-1}		Mass,
#	CCS	NH_3	CCS	NH_3	$\mathcal{M}_\odot$
6∗	3.50	3.43	0.07	0.09	3.1
12	3.47	3.20	0.19	0.15	20.4
14∗	3.45	3.47	0.09	0.14	9.7
40∗	3.35	3.30	0.06	0.10	9.2
42∗	3.86	3.75	0.11	0.11	2.8
87	4.50	4.47	0.25	0.14	10.3
89	4.87	4.45	0.26	0.10	1.4
92∗	5.04	5.10	0.12	0.19	1.6
93∗	5.26	5.17	0.17	0.17	3.5
101∗	3.37	3.31	0.07	0.09	1.9
102	4.84	4.87	0.08	0.24	6.7
109∗	5.80	5.75	0.07	0.08	3.6

same volume elements. However, in 5 out of 6 low-mass young star-forming regions studied in [52] the widths of the CCS lines are too narrow, $\sigma_v(\mathrm{CCS}) < 0.55\sigma_v(\mathrm{NH_3})$, which is consistent with both molecules tracing different regions of gas with different kinematics. The only exception in this sample is the B1-IRS cloud where the spatial anticorrelation in the CCS- and NH_3-emitting gas has been revealed [51]. On the other hand, from the survey of dense cores using lines of N_2H^+, C_3H_2, and CCS it was deduced [53] that velocities and linewidths of these three molecules are well correlated among themselves and with NH_3, indicating a kinematic consistency for these species.

The three strongest hyperfine components of the $J = 5 - 4$ rotational transition of HC_3N [54] were partly resolved in radio-astronomical observations [55]. HC_3N, as well as CCS, is abundant in the early stage of chemical evolution of the star-forming regions [56] when the ratio of the fractional abundances of HC_3N and CCS remains almost constant [47] and the spatial distributions of these C-bearing molecules match each other quite well. The continued chemical evolution leads, however, to the spatial variation of the relative molecular abundances (chemical differentiation) due to adsorption of the heavy elements from the gas phase onto grain mantles at high densities and dust temperatures $T_{\mathrm{D}} < 20$ K [33]. In the later stages of the protostellar collapse carbon chain molecules are destroyed by high velocity outflows and radiation from protostars, whereas the same processes favor the desorption of ammonia from dust grains [47].

Thus, the spatial distribution of the emitting gas tracers in star-forming regions is governed by both the physical conditions within the dense cores and the time-dependent chemistry. The consistency of the apparent linewidths of different molecules is a necessary condition for these molecules to be co-spatially distributed, but is not a sufficient one.

Molecular line profiles are also affected by the bulk kinematics of the dense clouds. Plane-of-sky bulk motions observed in starless cores exhibit velocity gradients of ∼0.3 to 1.4 km s^{-1} pc^{-1} [57, 58]. A differential rotation and angular momentum evolution in the B68 core with velocity gradients of 3.4 and 4.8 km s^{-1} pc^{-1} for the outer and inner material respectively was found in [59]. Similarly, the spatial variations of the velocity gradients in prestellar and protostellar cores of ∼2 km s^{-1} pc^{-1} [45] indicate deviations from simple solid body rotation.

The gas kinematics along the line-of-sights studied in the isolated cores [60] shows that cores move slowly ($\lesssim 0.1$ km s^{-1}) relatively to their surroundings. Inward and/or outward motion with velocity of ∼0.1 km s^{-1} is revealed by the skewed line profiles. For instance, blue asymmetry of the hyperfine components of the N_2H^+ (1-0) transition seen in two starless cores can be produced by absorption along the line-of-sight in the foreground inward-moving gas of lower excitation [61]. Acoustic type oscillations with amplitude of ∼0.1 km s^{-1} are seen in the inward and outward gas motion across the B68 core [59]. A redshifted peak of the CCS $3_2 - 2_1$ emission line of ∼0.16 km s^{-1} with respect to the central velocity of the NH_3 (1,1) line was detected in the L1551 dark cloud [58].

The turbulent component of the gas velocity derived in [44] from the intrinsic linewidths of the NH_3 and N_2H^+ lines is small and subsonic, $\sigma_{\mathrm{tur}} \lesssim 0.1$ km s^{-1} (for $T_{\mathrm{kin}} = 10$ K, sound speed is 0.19 km s^{-1}). Earlier, a similar conclusion has been obtained from NH_3 observations of low-mass dense cores [62].

The velocity widths in high-mass clumps associated with IRDCs are large (∼1-3 km s^{-1}) and indicate the supersonic motion. If the IRDCs are high-mass star-forming regions, then, as noted in Ref. [36], the observed

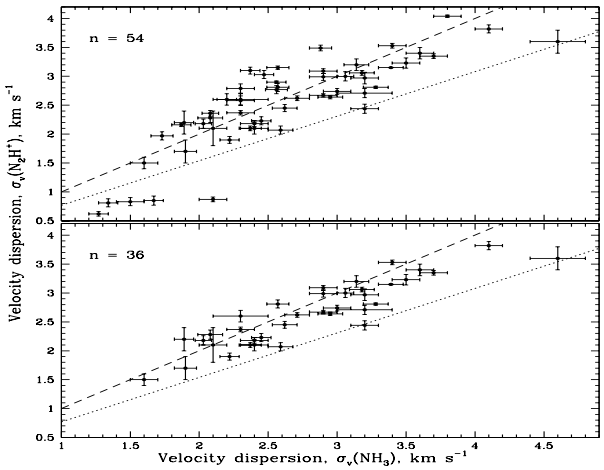

FIG. 4: *Upper panel*: N_2H^+ (1−0) versus NH_3(1,1) linewidths for massive clumps associated with infrared dark clouds from the survey of Ref. [36]. The error bars represent 1σ standard deviations. *Lower panel*: Same as the upper panel but for the points marked by asterisks in Table IV. In both panels, the dashed and dotted lines are the boundaries for, respectively, pure turbulent, $\sigma_v(N_2H^+) = \sigma_v(NH_3)$, and pure thermal, $\sigma_v(N_2H^+) = 0.77\sigma_v(NH_3)$, line broadening. The sample sizes are indicated in the panels.

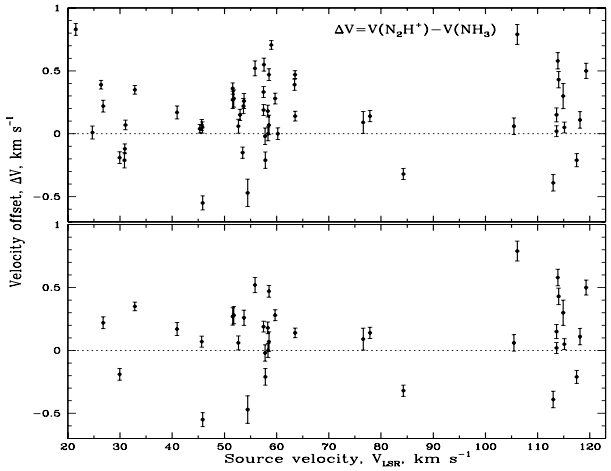

FIG. 5: *Upper panel*: Velocity offset $\Delta V_{N_2H^+ - NH_3}$ versus the source radial velocity set by $V_{LSR}(NH_3)$. *Lower panel*: Same as the upper panel but for the points marked by asterisks in Table IV. The vertical error bars include both random and systematic errors caused by the uncertainties of the adopted rest frequencies (Table I).

large velocity widths are consistent with a model which suggests massive star formation in turbulence-supported cores with a high accretion rate [63]. The innermost regions of such clumps are traced by molecular transitions with relatively large excitation energies of the upper states. To excite such transitions denser and hotter regions closer to the protostar are required. The NH_3 (2,2) and (3,3) transitions have, for example, the excitation energies of $E_u^{(2,2)} = 65$ K and $E_u^{(3,3)} = 125$ K, and so their velocity distributions should be broader than that of the NH_3 (1,1) line for which $E_u^{(1,1)} = 23$ K. We may expect that other molecules, such as CCS ($J_N = 2_1 - 1_0$), HC_3N ($J = 5 - 4$), and N_2H^+ ($J = 1 - 0$) with excitation energies lower than 23 K, would have velocity distributions similar to that of NH_3 (1,1).

III. RESULTS

As noted in the previous section, the observational constraint on $\Delta\mu/\mu$ is set by the velocity offset, ΔV, measured between the ammonia inversion line and a molecular rotational line, Eq.(3). In this comparison, to minimize possible systematics in the ΔV values, the second molecule must follow closely the spatial distribution of NH_3. The most favorable candidate which fits this condition is the molecular ion N_2H^+. As for carbon-chain molecules, it seems likely that CCS and HC_3N are anti-correlated with NH_3, albeit not all of the dense cores display chemical differentiation (Ref. 38, Sect. 4.4). When molecules trace the same gas, their turbulent component should be equal, and the lighter NH_3 should always have larger linewidth if turbulent and thermal line broadening are comparable, $\sigma_{tur}/\sigma_{therm} \sim 1$. If, however, the turbulent component dominates, the lines may have similar widths. We use this criterion to select molecular pairs tracing presumably the same gas velocity, i.e. arising co-spatially.

It is to note that the velocity offset ΔV in Eq.(3) is the sum of two components, $\Delta V = \Delta V_\mu + \Delta V_n$, with ΔV_μ being the shift due to μ-variation, and ΔV_n the shift induced by Doppler noise. Assuming the random character of the Doppler noise, the signal ΔV_μ can be estimated statistically by averaging over a large data sample. The validity of this assumption requires, however, additional tests as discussed below in Sect. III C.

A. Dense cores in the Perseus molecular cloud

At first we consider an ammonia spectral atlas of 193 dense protostellar and prestellar cores of low masses in the Perseus molecular cloud [34]. The spectral observations of the cores in NH_3 (1,1), (2,2), CCS ($2_1 - 1_0$) and $CC^{34}S$ ($2_1 - 1_0$) lines were carried out simultaneously using the 100-m Robert F. Byrd Green Bank Telescope (GBT). Each target was observed in a single-pointing, frequency-switched mode allowing the entire NH_3 (1,1) complex to remain within the spectral window. The GBT beam size at 23 GHz is $FWHM = 31''$ or 0.04 pc at the Perseus cloud distance ($D \sim 260$ pc). The resulting spectral resolution was 24 m s^{-1}. Thus, both molecules were observed with similar angular and spectral resolutions.

The typical cores in Perseus have the mean gas density $n_H \sim (1-2) \times 10^4$ cm^{-3}, velocity dispersion $\sigma_v = 0.17$ km s^{-1}, kinetic temperature $T_{kin} = 11$ K, radius $R = 0.09$ pc, and mass $\mathcal{M} \sim 1\ \mathcal{M}_\odot$. The Perseus molecular

TABLE IV: Parameters of massive clumps associated with infrared dark clouds taken from Ref. [36] and representing emission lines of N_2H^+ $(1-0)$ and NH_3 (1,1). Asterisk marks objects with $0.77\sigma_v(NH_3) \lesssim \sigma_v(N_2H^+) \lesssim \sigma_v(NH_3)$ (see Fig. 4, lower panel).

Source	$V_{\rm LSR}$, km s^{-1}		σ_v, km s^{-1}		D,
	N_2H^+	NH_3	N_2H^+	NH_3	*kpc*
G015.05+00.07 MM1	24.73(3)	24.72(4)	2.79(8)	2.3(1)	2.5
G015.31–00.16 MM2	31.12(2)	31.05(3)	0.81(7)	1.34(7)	3.1
G015.31–00.16 MM3	30.81(2)	30.93(3)	0.62(4)	1.27(7)	3.0
G019.27+00.07 MM1	26.76(1)	26.37(3)	3.15(3)	2.57(8)	2.3
G019.27+00.07 MM2∗	27.01(2)	26.79(4)	2.62(4)	2.71(9)	2.3
G022.35+00.41 MM1∗	52.73(2)	52.67(5)	2.74(5)	3.0(1)	3.7
G022.35+00.41 MM2	60.22(2)	60.22(4)	0.83(7)	1.5(1)	4.1
G022.35+00.41 MM3∗	83.97(3)	84.29(3)	2.23(7)	2.45(7)	5.3
G023.60+00.00 MM1∗	106.89(6)	106.10(5)	3.82(7)	4.1(1)	6.7
G023.60+00.00 MM2	53.34(3)	53.49(3)	3.03(7)	2.47(7)	3.7
G023.60+00.00 MM3∗	105.51(4)	105.45(5)	3.4(1)	3.6(1)	6.6
G023.60+00.00 MM4	53.87(5)	53.65(3)	2.6(1)	2.20(7)	3.7
G023.60+00.00 MM7∗	54.00(5)	53.74(3)	1.90(6)	2.22(7)	3.7
G024.08+00.04 MM1∗	113.63(1)	113.61(4)	2.67(3)	2.9(1)	7.8
G024.08+00.04 MM2(1)∗	52.08(3)	51.80(6)	1.5(1)	1.6(1)	3.6
G024.08+00.04 MM2(2)∗	114.45(4)	114.02(5)	2.1(1)	2.4(1)	7.8
G024.08+00.04 MM3∗	51.86(6)	51.59(3)	2.2(2)	1.89(7)	3.6
G024.08+00.04 MM4	51.95(3)	51.59(3)	0.85(8)	1.67(7)	3.6
G024.33+00.11 MM1∗	113.76(2)	113.61(5)	3.53(4)	3.4(1)	7.7
G024.33+00.11 MM2∗	118.22(4)	118.11(5)	3.23(9)	3.5(1)	7.7
G024.33+00.11 MM4∗	115.19(7)	114.89(7)	3.6(2)	4.6(2)	7.7
G024.33+00.11 MM5∗	117.26(4)	117.47(3)	3.0(8)	3.06(6)	7.7
G024.33+00.11 MM6∗	114.43(4)	113.85(5)	2.97(10)	3.2(1)	7.7
G024.33+00.11 MM9∗	119.78(5)	119.28(3)	1.7(2)	1.90(8)	7.7
G024.33+00.11 MM11∗	112.60(5)	112.99(4)	2.18(5)	2.4(1)	7.7
G024.60+00.08 MM1	53.14(3)	52.99(3)	3.10(6)	2.37(7)	3.6
G024.60+00.08 MM2∗	115.16(1)	115.11(4)	2.37(4)	2.3(1)	7.7
G025.04–00.20 MM1	64.00(2)	63.53(2)	2.36(5)	2.08(6)	4.2
G025.04–00.20 MM2	63.83(3)	63.44(3)	2.77(7)	2.56(8)	4.3
G025.04–00.20 MM4∗	63.69(2)	63.55(3)	2.18(8)	2.03(6)	4.1
G034.43+00.24 MM1∗	57.77(5)	57.79(4)	3.15(1)	3.39(9)	3.5
G034.43+00.24 MM2	57.832(9)	57.50(4)	4.04(2)	3.8(1)	3.5
G034.43+00.24 MM3	59.686(8)	58.98(3)	2.90(2)	2.56(7)	3.6
G034.43+00.24 MM4∗	57.689(8)	57.50(4)	2.81(2)	3.28(9)	3.5
G034.43+00.24 MM5	58.12(3)	57.57(4)	2.58(8)	2.3(1)	3.5
G034.43+00.24 MM6∗	58.49(2)	58.31(4)	2.07(7)	2.59(9)	3.6
G034.43+00.24 MM8∗	57.63(5)	57.84(4)	3.2(1)	3.14(9)	3.5
G034.43+00.24 MM9∗	59.00(2)	58.53(4)	2.45(6)	2.62(9)	3.6
I18102–1800 MM1	22.36(2)	21.53(4)	3.49(5)	2.88(8)	2.7
I18151–1208 MM1∗	33.19(1)	32.84(3)	2.10(4)	2.37(8)	2.8
I18151–1208 MM2∗	29.74(2)	29.93(4)	3.09(4)	2.9(1)	2.6
I18151–1208 MM3	30.65(1)	30.86(6)	0.87(4)	2.1(1)	2.7
I18182–1433 MM1∗	60.00(1)	59.72(4)	3.06(4)	3.18(9)	4.6
I18182–1433 MM2∗	41.10(3)	40.93(4)	2.28(8)	2.08(9)	3.6
I18223–1243 MM1	45.32(1)	45.28(3)	2.16(3)	1.87(7)	3.6
I18223–1243 MM2∗	45.29(2)	45.84(5)	2.99(6)	2.9(1)	3.6
I18223–1243 MM3∗	45.73(1)	45.66(4)	2.64(3)	2.95(9)	3.7
I18223–1243 MM4	45.83(3)	45.78(3)	1.97(7)	1.73(8)	3.7
I18306–0835 MM1∗	78.02(3)	77.88(3)	2.81(7)	2.57(8)	4.9
I18306–0835 MM2∗	76.67(5)	76.58(7)	2.6(1)	2.3(2)	4.9
I18306–0835 MM3∗	53.98(9)	54.45(6)	2.1(3)	2.1(1)	3.7
I18337–0743 MM1∗	58.37(2)	58.37(5)	3.35(4)	3.7(1)	3.9
I18227–0743 MM2∗	58.60(3)	58.53(7)	2.71(8)	3.2(2)	3.9
I18227–0743 MM3∗	56.37(3)	55.85(5)	2.44(8)	3.2(1)	3.8

cloud covers an area of 6 by 2 degrees (27×9 pc) and contains over $10^4\mathcal{M}_\odot$ of gas and dust that corresponds to the mean gas density of $n_{\rm H} \sim 4 \times 10^2$ cm^{-3}.

The atlas of 193 sources is very conveniently presented on the website (see Ref. 34 for details) where the original spectra are shown along with the best fitting models, model parameters and their uncertainties. These authors found that many cores show evidence for the multiple velocity components along the line-of-sight. The total number of cores where both CCS (2_1-1_0) and NH_3 (1,1) lines were detected is 98. The central velocities of these lines, being averaged with weights inversely proportional to the variances of the measurements, reveal that CCS lines are systematically offset by 16 m s^{-1}. It was suggested in Ref. [34] that this offset is due to uncertainties in the assumed rest frequency of the CCS line. A similar marginally significant offset in the velocities of the $C^{18}O$ (1-0) and NH_3 (1,1) lines was measured from 18 dark

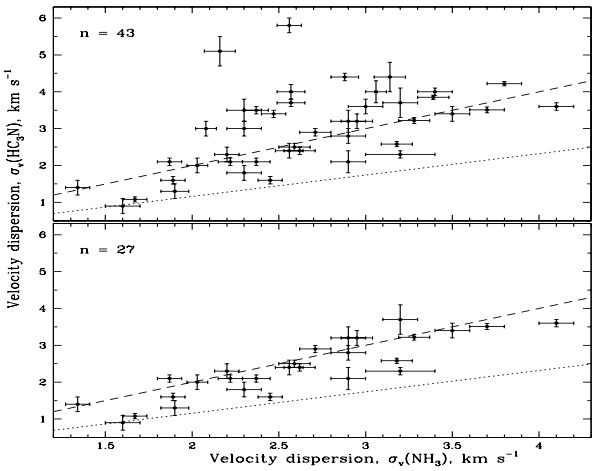

FIG. 6: Same as Fig. 4 but for HC_3N $(5-4)$ and $NH_3(1,1)$ linewidths. Points in the lower panel are marked by asterisks in Table V. In both panels the dashed and dotted lines are the boundaries for, respectively, pure turbulent, $\sigma_v(HC_3N) = \sigma_v(NH_3)$, and pure thermal, $\sigma_v(HC_3N) = 0.58\sigma_v(NH_3)$, line broadening. The sample sizes are indicated in the panels.

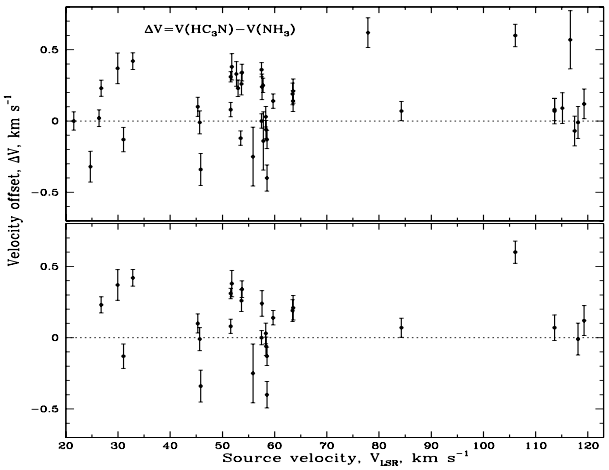

FIG. 7: Same as Fig. 5 but for emission lines HC_3N and NH_3. The total sample is shown in Fig. 6, upper panel. The points in the lower panel are those marked by asterisks in Table V.

cores in which the same position was observed in both NH_3 (1,1) and $C^{18}O$ (1-0) [41].

Figure 1, upper panel, shows linewidths of CCS $(2_1 - 1_0)$ vs. NH_3 (1,1) for a total sample of data points $(n = 98)$ from [34]. In this panel, the dashed and dotted lines are the boundaries for, respectively, pure turbulent, $\sigma_v(\mathrm{CCS}) = \sigma_v(NH_3)$, and pure thermal, $\sigma_v(\mathrm{CCS}) = 0.55\sigma_v(NH_3)$, line broadening. A wide scatter of points reveals the fact that for many cores a complex structure of line profiles hampers the accurate estimate of the linewidth. As a next step, we selected from the database only those profiles which have been perfectly fitted by a single component model. The obtained subsample of $n = 34$ pairs is shown in the lower panel in Fig. 1 with the corresponding fitting parameters listed in Table II which have been taken from the online database. The original ammonia data were re-reduced with additional small Doppler corrections to eliminate IF-to-IF variations (IF stands for Intermediate Frequency – a frequency to which the radio frequency is shifted as an intermediate step before detection in the backend), but there were no significant changes from the values derived from the original data set [35].

Formal calculations of the weighted means for the total sample and subsample give $\Delta V^w_{n=98} = 0.016 \pm 0.013$ km s^{-1} (which is in line with Ref. 34) and $\Delta V^w_{n=34} = 0.040 \pm 0.010$ km s^{-1}, respectively. However, to cancel out the Doppler noise component ΔV_n, simple (unweighted) averaging of data is more appropriate (as seen from Fig. 2, the ΔV values have approximately equal error bars). The corresponding unweighted values are $\Delta V_{n=98} = 0.044 \pm 0.013$ km s^{-1} and $\Delta V_{n=34} = 0.039 \pm 0.010$ km s^{-1}.

Now let us select only points with $\sigma_v(NH_3) > \sigma_v(\mathrm{CCS}) > 0.55\sigma_v(NH_3)$, i.e. points for which both emission lines arise most probably co-spatially (Fig. 1, lower panel). This gives $n = 21$ and $\Delta V^w_{n=21} = 0.050 \pm 0.013$ km s^{-1}, and $\Delta V_{n=21} = 0.048 \pm 0.013$ km s^{-1}.

The distributions of the selected points are shown in Fig. 2. Here the vertical error bars include both the error of the measurement and the systematic error of $\varepsilon_v = 13.5$ m s^{-1}, indicating approximate equidispersion of the individual measurements. It is clearly seen that points with positive offsets dominate. The scatter of the points reflects complexity of gas kinematics and effects of chemical segregation of one molecule with respect to the other in dense molecular cores discussed in Sect. II.

The unweighted mean from the $n = 21$ subsample will be considered as the final estimate of the velocity offset for the Perseus dark cores. Accounting for the systematic error due to uncertainties in the rest frequencies (Table I), we obtain $\Delta V_{n=21} = 0.048 \pm 0.013 \pm 0.0135$ km s^{-1}. The robust redescending M-estimate for the shift and scale [64] yields $\Delta V_{n=21} = 0.052 \pm 0.007 \pm 0.0135$ km s^{-1} (see our final Table VI).

To understand if there are subclasses among the Perseus cores, we also investigated the measured column densities of NH_3 and CCS. We found the mean ratio of $N(NH_3)/N(\mathrm{CCS}) = 1180 \pm 870$. There are only two outlying clouds with $N(NH_3)/N(\mathrm{CCS}) \sim 5500$ and 25000. The plot between the column density ratio versus velocity offset does not show any trend. It seems that the dark cores are rather homogeneous with respect to the column density ratio, and this probably means that there are no strong variations in abundances among the clouds. In other words there is no evidence for the two different populations.

TABLE V: Same as Table IV but for emission lines of HC_3N (5 − 4) and NH_3 (1,1). Asterisk marks objects with $0.58\sigma_v(NH_3) \lesssim \sigma_v(HC_3N) \lesssim \sigma_v(NH_3)$ (see Fig. 6, lower panel).

Source	V_{LSR}, km s^{-1}		σ_v, km s^{-1}		D,
	HC_3N	NH_3	HC_3N	NH_3	*kpc*
G015.05+00.07 MM1	24.4(1)	24.72(4)	3.5(3)	2.3(1)	2.5
G015.31–00.16 MM2∗	30.92(8)	31.05(3)	1.4(2)	1.34(7)	3.1
G019.27+00.07 MM1	26.39(5)	26.37(3)	3.7(1)	2.57(8)	2.3
G019.27+00.07 MM2∗	27.02(4)	26.79(4)	2.9(1)	2.71(9)	2.3
G022.35+00.41 MM1	53.00(7)	52.67(5)	3.6(2)	3.0(1)	3.7
G022.35+00.41 MM3∗	84.36(6)	84.29(3)	1.6(1)	2.45(7)	5.3
G023.60+00.00 MM1∗	106.70(6)	106.10(5)	3.6(1)	4.1(1)	6.7
G023.60+00.00 MM2	53.37(4)	53.49(3)	3.4(1)	2.47(7)	3.7
G023.60+00.00 MM4∗	53.91(7)	53.65(3)	2.3(2)	2.20(7)	3.7
G023.60+00.00 MM7∗	54.08(5)	53.74(3)	2.1(1)	2.22(7)	3.7
G024.08+00.04 MM1∗	113.68(8)	113.61(4)	2.8(2)	2.9(1)	7.8
G024.08+00.04 MM2(1)∗	52.18(7)	51.80(6)	0.9(2)	1.6(1)	3.6
G024.08+00.04 MM3∗	51.67(4)	51.59(3)	1.6(1)	1.89(7)	3.6
G024.08+00.04 MM4∗	51.90(2)	51.59(3)	1.08(7)	1.67(7)	3.6
G024.33+00.11 MM1	113.69(6)	113.61(5)	4.0(1)	3.4(1)	7.7
G024.33+00.11 MM2∗	118.1(1)	118.11(5)	3.4(2)	3.5(1)	7.7
G024.33+00.11 MM3	117.2(2)	116.63(4)	5.1(4)	2.16(9)	7.7
G024.33+00.11 MM5	117.4(1)	117.47(3)	4.0(3)	3.06(6)	7.7
G024.33+00.11 MM9∗	119.4(1)	119.28(3)	1.3(2)	1.90(8)	7.7
G024.60+00.08 MM1	53.22(5)	52.99(3)	3.5(1)	2.37(7)	3.6
G024.60+00.08 MM2	115.2(1)	115.11(4)	3.0(2)	2.3(1)	7.7
G025.04–00.20 MM1	63.67(7)	63.53(2)	3.0(2)	2.08(6)	4.2
G025.04–00.20 MM2∗	63.63(7)	63.44(3)	2.4(2)	2.56(8)	4.2
G025.04–00.20 MM4∗	63.76(8)	63.55(3)	2.0(2)	2.03(6)	4.1
G034.43+00.24 MM1	58.04(3)	57.79(4)	3.85(6)	3.39(9)	3.5
G034.43+00.24 MM2	57.86(3)	57.50(4)	4.22(6)	3.8(1)	3.5
G034.43+00.24 MM3	60.05(7)	58.98(3)	5.8(2)	2.56(7)	3.6
G034.43+00.24 MM4∗	57.50(3)	57.50(4)	3.22(8)	3.28(9)	3.5
G034.43+00.24 MM5∗	57.81(8)	57.57(4)	1.8(2)	2.3(1)	3.5
G034.43+00.24 MM6∗	58.34(6)	58.31(4)	2.5(1)	2.59(9)	3.6
G034.43+00.24 MM8	57.7(2)	57.84(4)	4.4(4)	3.14(9)	3.5
G034.43+00.24 MM9∗	58.40(5)	58.53(4)	2.4(1)	2.62(9)	3.6
I18102–1800 MM1	21.53(5)	21.53(4)	4.4(1)	2.88(8)	2.7
I18151–1208 MM1∗	33.26(5)	32.84(3)	2.1(1)	2.37(8)	2.8
I18151–1208 MM2∗	30.30(1)	29.93(4)	3.2(3)	2.9(1)	2.6
I18182–1433 MM1∗	59.86(3)	59.72(4)	2.58(7)	3.18(9)	4.6
I18223–1243 MM1∗	45.38(6)	45.28(3)	2.1(1)	1.87(7)	3.6
I18223–1243 MM2∗	45.5(1)	45.84(5)	2.1(3)	2.9(1)	3.6
I18223–1243 MM3∗	45.65(7)	45.66(4)	3.2(2)	2.95(9)	3.7
I18306–0835 MM1	78.5(1)	77.88(3)	4.0(2)	2.57(8)	4.9
I18337–0743 MM1∗	58.31(4)	58.37(5)	3.51(8)	3.7(1)	3.9
I18337–0743 MM2∗	58.13(6)	58.53(7)	2.3(1)	3.2(2)	3.9
I18337–0743 MM3∗	55.6(2)	55.85(5)	3.7(4)	3.2(1)	3.8

B. Dense cores in the Pipe Nebula

The second sample of molecular lines is based on high quality data from Ref. [65] who observed a starless population of 46 molecular cores in the Pipe Nebula ($D \sim 130$ pc). The Pipe Nebula is one of the closest molecular clouds with a mass of $10^4\mathcal{M}_\odot$ covering an area of 48 deg^2 on the sky.

The observations were performed with the 100-m Robert C. Byrd Green Bank Telescope (GBT). The NH_3 (1,1), (2,2), CCS ($2_1 - 1_0$), and HC_5N (9-8) transitions were observed simultaneously as in the case of the Perseus cloud (the frequency of the HC_5N $J = 9 - 8$ transition is 23.96 GHz, and its upper state excitation temperature $E_u^{(9,8)} = 5.8$ K). The GBT beam size of $\sim 30''$ provides the angular resolution of ~ 0.02 pc at the Pipe Nebula distance, i.e. the internal structure of dense cores ($R \simeq 0.09$ pc) was partly resolved. The velocity resolution was 23 m s^{-1}.

There are four sources in the Pipe Nebula sample (Nos. 12, 40, 101, 109 in Table 4 in Ref. 65) where both NH_3 (1,1) and HC_5N (9,8) lines are observed. The molecule HC_5N is 4.4 times heavier than NH_3, i.e. its lines should be intrinsically narrower than ammonia lines if molecules trace the same gas. However, each of these sources exhibits HC_5N velocity dispersion broader than NH_3: in average $\sigma_v(HC_5N) = (1.5 \pm 0.1)\ \sigma_v(NH_3)$. An even worse relationship is seen between HC_5N and CCS velocity dispersions: in average $\sigma_v(HC_5N) = (1.8 \pm 0.5)\ \sigma_v(CCS)$. This could be expected if NH_3 and CCS trace not all the gas along the line of sight but only a part associated with the dense compact core. However, not all of the 12 NH_3 and CCS emission sources listed in Table III show the expected correlation of the velocity dispersion. Four sources marked by open circles in Fig. 3, upper panel,

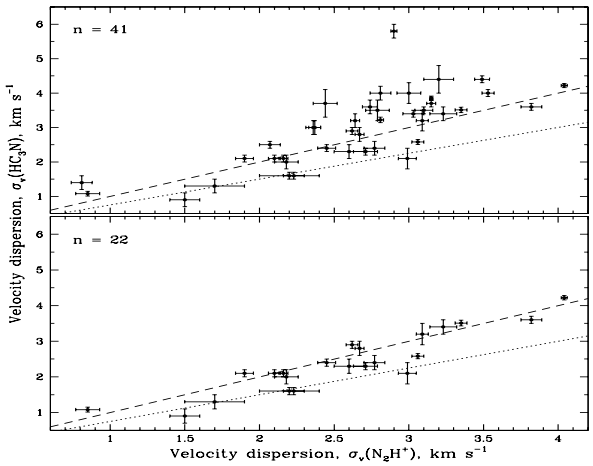

FIG. 8: *Upper panel*: HC_3N $(5-4)$ versus N_2H^+ $(1-0)$ linewidths for massive clumps associated with infrared dark clouds [36]. The error bars represent 1σ standard deviations. *Lower panel*: Same as the upper panel but for the points distributed between the dashed and dotted lines which constrain respectively pure turbulent, $\sigma_v(HC_3N) = \sigma_v(N_2H^+)$, and pure thermal, $\sigma_v(HC_3N) = 0.58\sigma_v(N_2H^+)$, line broadening. The sample sizes are indicated in the panels.

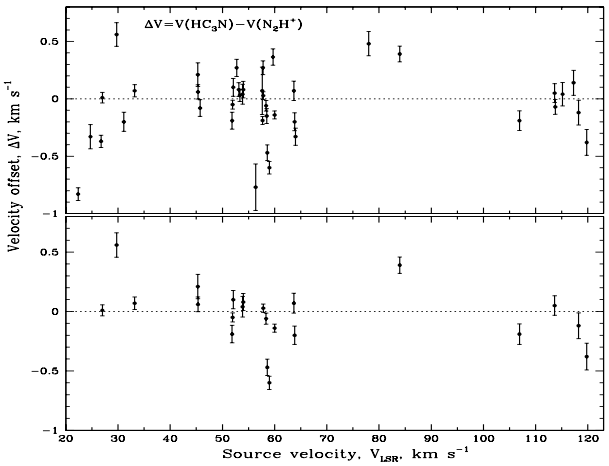

FIG. 9: *Upper panel*: Velocity offset $\Delta V_{HC_3N-N_2H^+}$ versus the source radial velocity set by $V_{LSR}(N_2H^+)$. *Lower panel*: Same as the upper panel but for the points from the lower panel in Fig. 8. The vertical error bars include both random and systematic errors caused by the uncertainties of the adopted rest frequencies (Table I).

are those where two species trace different regions. The distribution of the remaining 8 points is shown in Fig. 3, lower panel. Again, as for the sources from the Perseus molecular cloud, we find a positive offset in the radial velocities. The difference between the CCS and NH_3 velocity has the mean of $\Delta V_{n=8} = 0.044$ km s^{-1} and the standard deviation of 0.020 km s^{-1}. Adding the error of the rest frequencies, we obtain the final values $\Delta V_{n=8} = 0.044 \pm 0.020 \pm 0.0135$ km s^{-1}, and the robust M-estimate $\Delta V_{n=8} = 0.069 \pm 0.011 \pm 0.0135$ km s^{-1} (Table VI).

C. Massive clumps associated with Infrared Dark Clouds

The third example deals with more distant objects — cold, dense, and massive clumps ($\mathcal{M} > 100\mathcal{M}_\odot$) of 1-10 pc sizes associated with the IRDCs which are located at distances larger than 2 kpc and seen in silhouette against the bright diffuse mid-infrared emission of the Galactic plane. The gas kinetic temperature of IRDCs is as low as the temperature of the dense molecular cores, $T_{\rm kin} < 20$ K [66]. This means that massive clumps in IRDCs are either starless or in a very early stage of high-mass star formation.

A recent survey of 55 massive clumps in NH_3 (1,1), (2,2), (3,3), N_2H^+ (1-0), and HC_3N (5-4) lines has been carried out at the Nobeyama Radio Observatory 45-m telescope [36]. The N_2H^+ and HC_3N (5-4) lines (Table I) were observed simultaneously using two SIS receivers. The third receiver HEMT was used for NH_3 lines. The data were obtained within one day for each position, and different receivers used in these observations allow the Doppler tracking to be completely independent between these molecular lines [37].

The angular and velocity resolutions in these observations were different. At the frequencies of the NH_3, HC_3N, and N_2H^+ transitions the half-power beam width was $73''$, $37''$, and $18''$, and the velocity resolution was 0.50, 0.25, and 0.12 km s^{-1}, respectively. At a distance of $\sim$5 kpc the spatial structures of $\sim$1.8, 0.9, and 0.4 pc can be resolved in, correspondingly, NH_3, HC_3N, and N_2H^+ lines. The inhomogeneity of the observational parameters and significant turbulence in IRDC cores ($\sigma_{\rm turb} \sim 1-3$ km s^{-1}) increase the dispersion of the Doppler noise in massive clumps as compared with low-mass molecular cores.

Table IV lists 54 sources from [36] where both N_2H^+ (1-0) and NH_3 (1,1) lines were detected. These molecules are expected to have similar spatial distributions. However, Fig. 4, upper panel, shows that some of the N_2H^+ lines have either too large or too small velocity dispersion as compared to NH_3, which may be related to a large angular resolution difference ($18''$ vs. $73''$) in observations of these molecules. Such points were excluded from the sample, the remaining $n = 36$ points are presented in Fig. 4, lower panel. The velocity offset distributions from the total sample and the subsample are shown in Fig. 5, upper and lower panels, respectively. The weighted and unweighted means are as follows: $\Delta V^w_{n=36} = 0.124 \pm 0.043$ km s^{-1}, and $\Delta V_{n=36} = 0.122 \pm 0.049$ km s^{-1}. In this case the laboratory error is equal to $\varepsilon_v = 13.6$ m s^{-1}. For the final estimate we take the more appropriate unweighted mean $\Delta V_{n=36} = 0.122 \pm 0.049 \pm 0.0136$ km s^{-1}, and the robust M-estimate $\Delta V_{n=36} = 0.160 \pm 0.032 \pm 0.0136$ km s^{-1} (Table VI).

TABLE VI: Sample mean values (unweighted) ΔV, standard deviations $\sigma_{\rm rms}$, robust M-estimates of the sample mean ΔV_M, and the scale σ_M deduced from the original data and from the subsamples of molecular lines showing self-consistent linewidths. Col. 9 lists velocity offsets corrected for uncertainties of the rest frequencies (see Sect. IV A for more details). The errors of the mean $\sigma_{\rm rms}/\sqrt{n}$ and $\sigma_M/\sqrt{n}$ are listed, respectively, in columns (4) and (6).

Object	Molecular pair	Sample size, n	ΔV, km s^{-1}	$\sigma_{\rm rms}$, km s^{-1}	ΔV_M, km s^{-1}	σ_M, km s^{-1}	$\varepsilon_{{\rm sys},\Delta V}$ km s^{-1}	$\Delta V_M^{\rm corr}$, km s^{-1}
(1)	(2)	(3)	(4)	(5)	(6)	(7)	(8)	(9)
Perseus	NH_3/CCS	98	0.044 ± 0.013	0.129	0.040 ± 0.007	0.073	0.0135	0.024
		34	0.039 ± 0.010	0.058	0.045 ± 0.007	0.043	0.0135	0.029
		21	0.048 ± 0.013	0.060	0.052 ± 0.007	0.032	0.0135	0.036
Pipe	NH_3/CCS	12	0.087 ± 0.039	0.135	0.039 ± 0.023	0.081	0.0135	0.023
		8	0.044 ± 0.020	0.057	0.069 ± 0.011	0.030	0.0135	0.053
IRDCs	NH_3/N_2H^+	54	0.157 ± 0.040	0.294	0.160 ± 0.030	0.220	0.0136	0.148
		36	0.122 ± 0.049	0.294	0.160 ± 0.032	0.190	0.0136	0.148
	NH_3/HC_3N	43	0.138 ± 0.043	0.282	0.110 ± 0.032	0.210	0.0031	0.105
		27	0.105 ± 0.045	0.234	0.120 ± 0.037	0.190	0.0031	0.115
	N_2H^+/HC_3N	41	-0.056 ± 0.047	0.301	-0.020 ± 0.037	0.240	0.0138	-0.013
		22	-0.033 ± 0.055	0.258	-0.017 ± 0.034	0.160	0.0138	-0.010

The correlation between velocity dispersions of the HC_3N (5-4) and NH_3 (1,1) emission lines is shown in Fig. 6. In this case the results were obtained with more comparable angular resolutions ($37''$ vs. $73''$). The total sample of the HC_3N/NH_3 pairs ($n = 43$) is given in Table V. Several of the measured HC_3N linewidths demonstrate significant supersonic turbulence of the emitting gas with $\sigma_v(HC_3N) > \sigma_v(NH_3)$. Such lines were omitted from the following analysis, the remaining $n = 27$ points are shown in Fig. 6, lower panel (the selected points are marked by asterisks in Table V, first column). Fig. 7 illustrates the distribution of the measured offsets. The calculated statistics are as follows: $\Delta V^w_{n=27} = 0.147 \pm 0.039$ km s^{-1}, and $\Delta V_{n=27} = 0.105 \pm 0.045$ km s^{-1}. Again, taking the unweighted estimate and accounting for the systematic error of $\varepsilon_v = 3.1$ m s^{-1} we come to the final mean value of the velocity offset $\Delta V_{n=27} = 0.105 \pm 0.045 \pm 0.0031$ km s^{-1}, and the robust M-estimate $\Delta V_{n=27} = 0.120 \pm 0.037 \pm 0.0031$ km s^{-1} (Table VI).

The data from Ref. [36] allow us to answer the question whether the revealed positive velocity offsets are related to ammonia lines or not. Following the same procedure as above, we can compare the velocities obtained from the sources which were observed in both N_2H^+ and HC_3N. The total sample of $n = 41$ pairs is shown in Fig. 8, upper panel. The heavier molecule HC_3N should have linewidths smaller or equal to that of N_2H^+. However, a considerable number of points ($\sim$50%) lie above the dashed line constraining pure turbulent line broadening. This is expected since N_2H^+ molecule traces more compact central regions of the dense clouds. The $n = 22$ points which presumably trace the same gas are shown in Fig. 8, lower panel. The corresponding velocity offset distributions are shown in Fig. 9. The mean values are $\Delta V^w_{n=22} = -0.053 \pm 0.044$ km s^{-1}, and $\Delta V_{n=22} = -0.033 \pm 0.055$ km s^{-1}, and thus the final estimates are $\Delta V_{n=22} = -0.033 \pm 0.055 \pm 0.0138$ km s^{-1}, and the robust M-value $\Delta V_{n=22} = -0.017 \pm 0.034 \pm 0.0138$ km s^{-1} (Table VI).

In this case both weighted and unweighted values are consistent with zero velocity offset. Since N_2H^+ and NH_3 share similar physical conditions in their formation and destruction processes and, hence, trace each other in spatial distributions, the obtained result indicates that ammonia is a key element responsible for the revealed velocity offset.

To demonstrate that the positive velocity offset does not result from our selection criterion we summarize all measurements complemented by robust redescending M-estimates for the shift and scale in Table VI. Both results are in good agreement within the 1σ uncertainty interval. The sample mean values reproduce a marginally significant signal ($\gtrsim 3\sigma$) independently on the sample size. When ammonia lines are excluded from the analysis, the signal disappears.

IV. DISCUSSION

In the previous section we showed that different molecular clouds demonstrate statistically significant velocity offset between the ammonia inversion transition $(J, K) = (1, 1)$ and rotational transitions of other molecules. Here we consider possible reasons of this offset.

A. Uncertainties of the rest frequencies

In cold dark clouds with the kinetic temperature $T_{\rm kin} \sim 10$K the thermal line broadening is very small ($v_{\rm th} \sim 50$ m s^{-1} for, e.g., CCS). This means that the detailed study of velocity offsets requires accuracy of rest frequencies of about 1 m s^{-1} [67]. Among molecules used in the present work only NH_3 fulfills this requirement. The hyperfine

TABLE VII: Hyperfine components of the HC_3N $J = 5 - 4$ transition. For Möller (Ref. 71), Yamamoto (Ref. 55), and JPL frequencies only the numbers after the decimal point are shown, the integer part is as in Lapinov's data [68]. Col. 10 and 11 list velocity offsets between Yamamoto and Lapinov (Y–L) and between JPL and Lapinov (JPL–L) values.

Transition					Rest Frequency (MHz)				Δv (m s^{-1})	
J'	F'	J	F	Weight	Lapinov	Möller	Yamamoto	JPL	Y–L	JPL–L
(1)	(2)	(3)	(4)	(5)	(6)	(7)	(8)	(9)	(10)	(11)
5	5	4	5	0.034	45488.83643(42)	.8368(10)				
5	4	4	3	0.658	45490.26138(42)	.2614(5)	.263(1)	.2580(3)	10.7	−22.3
5	5	4	4	0.812	45490.31378(42)	.3137(5)	.316(1)	.3102(3)	14.6	−23.6
5	6	4	5	1.000	45490.33740(42)	.3373(6)	.341(1)	.3336(4)	23.7	−25.0
5	4	4	5	0.0003	45490.63123(43)	.6317(16)				
5	4	4	4	0.034	45492.10858(42)	.1085(9)				

structure of the observed $(J, K) = (1, 1)$ transition of NH_3 is known with the accuracy of $\simeq 0.6$ m s^{-1} [69]. The available laboratory uncertainties for other molecules are significantly larger. Besides, there are shifts between rest frequencies reported in different publications. Below we estimate such systematics and their effect on the mean values of the velocity offsets obtained in Sect. III.

The frequency 22.344033 GHz of the CCS $J_N = 2_1 - 1_0$ transition (Table I) used in Refs. [34, 65] was calculated from a comparison with the three strongest hyperfine components of the HC_3N $J = 5 - 4$ transition observed towards a cold dark cloud L1498 assuming that the spatial distribution of CCS is the same as that of HC_3N [55]. According to Ref. [55], the $V_{\rm LSR}$ value obtained from the HC_3N transition was used to determine the frequencies of the CCS transitions without any corrections, and the frequencies of the CCS transitions were calculated from Gaussian fitting of the observed profiles. The error of 1 kHz indicated in Table I corresponds to one standard deviation obtained in the fit. However, up to now the $J = 5 - 4$ transition has not been measured in laboratory. The analysis of all available laboratory data on HC_3N carried out in Refs. [70, 71] and independently in Ref. [68] shows systematic frequency shifts (Table VII) with respect to the data presented in Ref. [55] and in the JPL Catalog (http://spec.jpl.nasa/gov/). On the other hand both Ref. [68] and Ref. [71] frequencies are in good agreement with the former having slightly better accuracy ($\varepsilon_v \simeq 2.8$ m s^{-1}). The mean value for the shift between rest frequencies used in Ref. [55] and calculated in Ref. [68] is $\Delta V_{\rm shift} = 16$ m s^{-1} (Col. 10, Table VII). Thus, the presented in Table VI robust M-estimates of the velocity offsets between CCS and NH_3 towards the Perseus molecular cloud and the Pipe Nebula corrected for this systematic shift will be $\Delta V^{\rm corr}_{n=21} = \Delta V_{n=21} - \Delta V_{\rm shift} = 0.036 \pm 0.007 \pm 0.0135$ km s^{-1}, and $\Delta V^{\rm corr}_{n=8} = \Delta V_{n=8} - \Delta V_{\rm shift} = 0.053 \pm 0.011 \pm 0.0135$ km s^{-1}, respectively (Table VI, Col. 9).

Now let us consider the IRDCs from Ref. [36]. In this measurements the lower spectral resolution does not allow to resolve hyperfine structure of the HC_3N $J = 5 - 4$ transition. The spectra of the HC_3N lines were fitted to a single Gaussian function and the corresponding radial velocities were calculated on base of a single hyperfine line $J = 5 - 4, F = 5 - 4$ [37] with the frequency 45490.3102 MHz taken from the JPL Catalog (Table VII, Col. 9). As a result, a small systematic shift due to unresolved hyperfine components was introduced. Its value can be estimated if we consider the center of gravity for the weighted central hyperfine components of the $J = 5 - 4$ transition listed in Table VII. The frequency of the center of gravity is $\nu_{\rm c.g.} = 45490.3058$ MHz and thus $\Delta V_{\rm c.g.} = 29$ m s^{-1}. However, as seen from Table VII (Col. 9), the JPL frequencies are systematically shifted with respect to Ref. [68] data and the mean value of the shift is $\Delta V_{\rm shift} = -23.6$ m s^{-1} (Col. 11). Combining both shifts, we obtain a correction of 5.4 m s^{-1}. This means that the velocity offset between HC_3N and NH_3 listed in Table VI should be as follows: $\Delta V^{\rm corr}_{n=27} = 0.115 \pm 0.037 \pm 0.0031$ km s^{-1} (Table VI, Col. 9).

The rest frequencies for the second molecule N_2H^+ observed towards the IRDCs Ref. [36] were taken from Ref. [42]. The hyperfine frequencies of the N_2H^+ $J = 1 - 0$ transition were estimated from observations of a molecular cloud L1512 in Taurus in both N_2H^+ (93 GHz) and C_3H_2 (85 GHz) lines assuming that the C_3H_2 and the N_2H^+ have exactly the same radial velocity. The absolute frequencies of the N_2H^+ hyperfine transitions measured in Ref. [42] are known with precision of ~ 7 kHz. However, a factor of two more accurate data are given in the Cologne Database for Molecular Spectroscopy (CDMS) described in Refs. [70, 71]. Both datasets are compared in Table VIII. The error of 4 kHz ($\varepsilon_v \simeq 13.5$ m s^{-1}) reported in Table I corresponds to the CDMS. The mean shift between the data from Ref. [42] and the CDMS frequencies is $\Delta V_{\rm shift} = 12$ m s^{-1}. Thus, the velocity offset between N_2H^+ and NH_3 from Table VI should be corrected to $\Delta V^{\rm corr}_{n=36} = \Delta V_{n=36} - 0.012 = 0.148 \pm 0.032 \pm 0.0136$ km s^{-1}, and between HC_3N and N_2H^+ to $\Delta V^{\rm corr}_{n=22} = \Delta V_{n=22} + 0.0066 = -0.010 \pm 0.034 \pm 0.0138$ km s^{-1} (Table VI, Col. 9).

TABLE VIII: Hyperfine components of the N_2H^+ $J = 1 - 0$ transition. For Caselli (Ref. 42) frequencies only the numbers after the decimal point are shown, the integer part is as in the Möller data (Ref. 71). Col. 10 lists velocity offsets between Caselli and Möller (C–M) values.

Transition							Rest Frequency (MHz)†		Δv (m s^{-1})
J'	F_1'	F'	J	F_1	F	Weight	Möller	Caselli	C–M
(1)	(2)	(3)	(4)	(5)	(6)	(7)	(8)	(9)	(10)
1	1	0	0	1	1	0.143	93171.6171(41)	.6210(70)	12.5
1	1	2	0	1	2	0.604	93171.9129(42)	.9168(70)	12.5
1	1	2	0	1	1	0.111	93171.9129(42)		
1	1	1	0	1	0	0.218	93172.0499(42)	.0533(70)	10.9
1	1	1	0	1	2	0.159	93172.0499(42)		
1	1	1	0	1	1	0.051	93172.0499(42)		
1	2	2	0	1	1	0.604	93173.4748(42)	.4796(70)	15.4
1	2	2	0	1	2	0.111	93173.4748(42)		
1	2	3	0	1	2	1.000	93173.7722(41)	.7767(70)	14.5
1	2	1	0	1	1	0.278	93173.9657(43)	.9666(70)	2.9
1	2	1	0	1	0	0.134	93173.9657(43)		
1	2	1	0	1	2	0.017	93173.9657(43)		
1	0	1	0	1	2	0.252	93176.2611(43)	.2650(70)	12.5
1	0	1	0	1	1	0.100	93176.2611(43)		
1	0	1	0	1	0	0.076	93176.2611(43)		

B. Systematics due to kinematic shifts

Spectroscopic measurement of the absolute radial velocities at the level of $50 - 100$ m s^{-1} is subject to many physical effects [72]. Fortunately, relative radial velocities are less sensitive to most of them. However, some small systematic shifts, in addition to those discussed in Sect. II, may be present in the measured values of ΔV.

First of all, the measurement of the relative radial velocities between two molecules requires the use of a common reference frame. In radio-astronomical observations it is usually the Local Standard of Rest (LSR). The transformation of the apparent Doppler velocity to $V_{\rm LSR}$ introduces an error of $\sim 1 - 3$ m s^{-1}, stemming from the following corrections: the observer's motion due to (1) the Sun's motion with respect to the LSR, (2) revolution of the Earth-Moon barycenter round the Sun, (3) motion of the Earth center round the Earth-Moon barycenter, and (4) rotation of the Earth [73]. This error ought to be added to the total error budget along with the systematic errors listed in Table VI, $8th$ column if molecular lines were not observed simultaneously.

The second error arises from gravitational shifts of the spectral lines due to the annual variation of the observer's distance from the Sun because of the eccentricity ($e \simeq 0.01671$) of the Earth's orbit ($A = 1$ AU). This produces the peak-to-peak variation of the radial velocity (in units of the speed of light, c) of

$$\delta V_{\rm g} = \frac{2eG\mathcal{M}_\odot}{Ac^2}\,. \tag{4}$$

The numerical value of $\delta V_{\rm g}$ is about 10 cm s^{-1}, and in our case this error can be neglected.

If we further define the dimensionless gravitational potential of the Sun on the Earth's orbit as (negative sign is omitted)

$$\Phi_0 = G\mathcal{M}_\odot/(Ac^2) + G\mathcal{M}_\oplus/(R_\oplus c^2) \simeq 1.06 \times 10^{-8}\,, \tag{5}$$

then the gravitational redshift for photons escaping an object of mass $\mathcal{M}$ and radius R scales as

$$\delta V_{\rm g} = \left(\frac{\mathcal{M}}{\mathcal{M}_\odot}\right)\left(\frac{A}{R}\right)\Phi_0\,. \tag{6}$$

Different gravitational redshifts between molecular lines may occur from the chemical stratification in dense molecular cores. However, this effect is negligible because of a relatively low gas density and rather large linear sizes of the clouds. For a typical starless core shown in Fig. 3 in Ref. [38], the gravitational velocity shifts of NH_3 and CCS lines are ~ 0.2 cm s^{-1} and ~ 0.1 cm s^{-1}, respectively.

Systematically redshifted CCS $2_1 - 1_0$ lines with respect to the NH_3 (1,1) central velocity may occur in contracting clouds when the near side of the external shell of the cloud with the CCS emission is moving towards the higher density core as suggested for, e.g, the L1551 dark cloud [58]. However, as discussed in Sect. II, in dark clouds both kinds of kinematic shifts (redward and blueward) are observed. Such bulk motions should randomize the Doppler shifts and provide a zero offset for a large size sample of dark clouds. Besides, all molecular cores in the Perseus molecular cloud are probably optically thin in the CCS $2_1 - 1_0$ emission since $CC^{34}S$ was not detected along any of the lines-of-sight [34] and $^{32}S : {}^{34}S = 22 : 1$. This means that the CCS emission line profile is formed in the whole volume of the cloud including both its near and distant sides. This is not the case, however, for the NH_3 emission. The total opacity in the (1,1) line transition varies between 0.84 and 10.9 for the cores listed in Table II. The optically thick clouds may cause some systematics of both signs (positive or

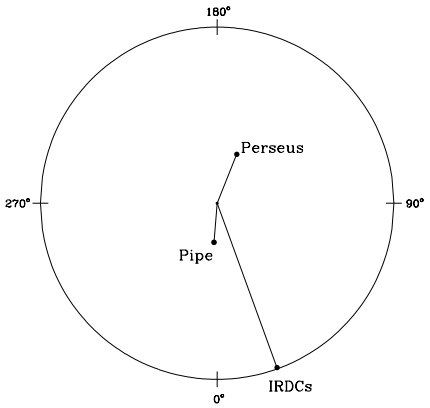

FIG. 10: Schematic location of the Perseus molecular cloud ($\ell \sim 158^\circ$, $b \sim -20^\circ$, $D \sim 260$ pc), the Pipe Nebula ($\ell \sim 356^\circ$, $b \sim 7^\circ$, $D \sim 130$ pc), and the IRDCs ($\ell \sim 15^\circ - 30^\circ$, $b < 1^\circ$, $D > 2$ kpc) in projection onto the Galactic plane. The Galactic center longitude is $\ell = 0^\circ$, by definition. Note that the distance to the IRDCs is not scaled and they lay much further out.

negative depending on the character of the internal bulk motions within the core) in the central positions of the NH_3 lines. However, three cores with $\tau_{(1,1)} \lesssim 1$ (Nos. 20, 112, and 151) demonstrate positive velocity offsets with the mean value of $\sim$100 m s^{-1}.

Among analyzed clouds the most accurate measurements of ΔV belong to the Perseus cores. We may use the M-estimate from the $n = 21$ sample (Sect. IV A) as a tentative value for the found velocity offset, $\Delta V = 36 \pm 7_{\rm stat} \pm 13.5_{\rm sys}$ m s^{-1}, or $\Delta V = 36 \pm 15$ m s^{-1} (1σ C.L.). Thus, the considered systematics do not explain the revealed offset. Assuming that this offset is caused entirely by the change of μ, one obtains from Eq.(3) $\Delta\mu/\mu = (3.5 \pm 1.4) \times 10^{-8}$, or $|\Delta\mu/\mu| < 5 \times 10^{-8}$. This is the most accurate estimate of $\Delta\mu/\mu$ based on the spectral analysis of astronomical objects. Next we consider whether this value is in line with other constraints.

C. Gravitational-potential dependence of μ

First we explore the dependence of the electron and proton masses on the strength of the gravitational potential. Theoretical models dealing with variations of physical constants do not require the cosmological temporal evolution of α and/or μ to be dominated over their local spatial changes in the Milky Way. For instance, theories like that of Ref. [74] consider direct coupling between the local matter density and the scalar fields that drive varying constants. The spatial change of the constants in these models is proportional to the local gravitational potential and the rate of spatial variation may exceed the rate of time variation (see, e.g., Ref. 30 and references cited therein). The effect of scalar fields on μ is additive (similar to gravity) and can be expressed as (Refs. 75, 76):

$$\frac{\Delta\mu}{\mu} = k_\mu \Delta\Phi \ , \qquad (7)$$

where k_μ is a dimensionless coupling constant of a massless (very light) scalar field to the local gravitational potential Φ, and $\Delta\Phi$ is the difference of the gravitational potentials between two measurement points.

This class of models suggests that the coupling of the scalar field φ to baryonic matter and fields is not too strong since otherwise it would produce a scalar-mediated 'fifth force' that is not observed [26]. It is also assumed that the φ-mediated force is a long-range one.

The respective contribution from the Galactic gravitational potential $\Phi_{\rm G}(r,\zeta)$ and the molecular cloud gravitational potential $\Phi_{\rm cloud}$ to the local gravitational potential is the sum

$$\Phi(r,\zeta) = \Phi_{\rm G}(r,\zeta) + \Phi_{\rm cloud} \ , \qquad (8)$$

where r and ζ denote two of the cylindrical coordinates.

The gravitational potential of IRDCs ($\mathcal{M} \sim 100\mathcal{M}_\odot$, $R \sim 1$ pc) and starless cores ($\mathcal{M} \sim 10\mathcal{M}_\odot$, $R \sim 0.1$ pc) is much smaller than that of the Sun on the Earth's orbit, Φ_0, namely, $\Phi_{\rm cloud} \sim 1/2000\ \Phi_0$. The value of $\Phi_{\rm G}(r,\zeta)$ can be calculated from analytic models of the Milky Way [77, 78, 79] which describe fairly well the galactic rotation curves. The galactic coordinates of the analyzed clouds are shown in Fig. 10. The distance of the Sun from the center of the Milky Way is $r_0 = 7.94 \pm 0.42$ kpc [80]. The Perseus molecular cloud is located towards the galactic anti-center, whereas the Pipe Nebula and the IRDCs in the direction of the galactic center. Between 3 and 8 kpc the galactic potential is about 2×10^{-6}, and $\Phi_{\rm G}$ changes within this interval very slowly: $\Delta\Phi_{\rm G} \sim 10^{-7}$.

With $\Delta\mu/\mu = 3.5 \times 10^{-8}$, one obtains $k_\mu \sim 1$, which is in sharp contradiction with estimates based on atomic clock experiments: $k_\mu = (-1.1 \pm 1.7) \times 10^{-5}$ [22]. There are two possible explanations for such a large discrepancy:

1. The measured velocity offset is mainly due to kinematic shifts. Then, taking the atomic clock limit $|k_\mu| < 3 \times 10^{-5}$ and the change of the galactic gravitational potential $\Delta\Phi \sim 10^{-7}$, one obtains from Eq. (7) an upper limit on $|\Delta\mu/\mu| \lesssim 10^{-12}$. Unfortunately, the level of 10^{-12} is below the precision of modern astronomical observations of molecular lines.

2. The electron-to-proton mass ratio does not linearly correlate with metric variations, i.e., $k_\mu \equiv 0$ in Eq. (7). The nonzero velocity offset is then caused by the change of the electron and proton masses. The corresponding theoretical background for this item is discussed below.

D. Dependence of μ on matter density

A class of models where baryon masses and coupling constants are strongly dependent on the local matter density, ρ, and where spatial variations of $\mu(\rho)$ and $\alpha(\rho)$ can be more pronounced than the temporal cosmological variations was considered in a number of publications discussed in Ref. [30]. In this approach it is suggested that the coupling of a scalar field to matter is much stronger than gravitational, but the fifth force problem does not arise since the linear coupling of the scalar field to matter is effectively suppressed by the matter density itself. The dynamics of the scalar field in these models depends on ρ: in low-density environments it is determined by the scalar field potential $V(\varphi)$, whereas in high-density regions (like the Earth's surface) it is set by the matter-φ coupling. The range of the scalar-mediated force for the terrestrial matter densities is then very short, less than 1 mm [30].

Because of the strong φ-coupling to matter the measurements of the frequency drifts in the atomic clock experiments ought to be insensitive to the changes in the gravitational potential at Earth caused by the eccentricity of Earth's orbit. The minimum of $V(\varphi)$ would show no shifts and $\Delta\alpha/\alpha$ ($\Delta\mu/\mu$) would be zero with good accuracy. However, comparison of atomic clocks at high altitude satellite orbits with laboratory clocks may yield useful constraints on model parameters as discussed in [30] who also suggested to test spatial variations of the physical constants through atomic and molecular line observations of the interstellar clouds in our galaxy. In this case the difference of matter densities between the terrestrial environment ($\rho_\oplus \sim 3\times10^{24}$ GeV cm^{-3}) and, e.g., dense molecular cores ($\rho_{\rm cloud} \sim 3\times10^{5}$ GeV cm^{-3}) may cause a shift in the expectation value of the scalar field φ_m leading to a change in masses and coupling constants.

If we interpret the nonzero offset of $\Delta V \sim 40$ m s^{-1} in terms of the change of fermion masses, then for low density environments, such as the interstellar clouds, the change in the electron-to-proton mass ratio is given by [30]:

$$\frac{\Delta\mu}{\mu} \simeq (\xi_{\rm e} - \xi_{\rm p})\ \frac{\varphi_m^2}{2}\ . \qquad (9)$$

In this model the scalar field is coupled to the standard model fermions through the dimensionless constants $\xi_{\rm e}$ and $\xi_{\rm p}$, with $\xi_{\rm p}$ being normalized to one.

The factor $(\xi_{\rm e}-1)$ can be much larger than unity in accord with astrophysical constraints discussed in [30]. If we assume that $(\xi_{\rm e}-1)/2 \gtrsim 1$, then $\varphi_m^2 \lesssim 3.5\times10^{-8}$, or $\varphi_m \lesssim 2\times10^{-4}$.

Thus, considered observations of the interstellar molecular clouds being interpreted in terms of the $\Delta\mu/\mu$ variation are in agreement with models which treat the φ-mediated force as a short-range force depending on the matter density. In accord with model predictions, the estimated value of the scalar field is much less than one. The measured spatial variation of $\Delta\mu/\mu$ does not contradict the laboratory studies on atomic clocks (see Sect. IV C) since extremely different density environment in the terrestrial measurements and in the interstellar medium prohibits direct comparison of the obtained results.

There are several extragalactic measurements of $\Delta\mu/\mu$ in which gas densities similar to those in the Milky Way clouds are observed. These results, being interpreted in terms of the spatial variations of $\Delta\mu/\mu$, can be compared with our estimate of $\Delta\mu/\mu = (3.5\pm1.4)\times10^{-8}$: it is consistent with the limit on $|\Delta\mu/\mu| < 3\times10^{-6}$ derived from the NH_3-bearing clouds at $z = 0.68$ [19], but in conflict with the value $\Delta\mu/\mu = (-24\pm6)\times10^{-6}$ obtained from molecular hydrogen H_2 absorption lines at $z \sim 3$ [16]. However, the same H_2-bearing clouds at $z \sim 3$ as analyzed in Ref. [16] were studied in Ref. [17]. The variability of μ was not confirmed at the level of $|\Delta\mu/\mu| \leq 4.9\times10^{-5}$. Recently a more stringent limit on $\Delta\mu/\mu$ was found at $z \sim 3$ in Ref. [18]: $\Delta\mu/\mu = (2.6\pm3.0)\times10^{-6}$. Since at densities as low as observed in the interstellar medium the dependence of μ on ρ is extremely weak, the value of $\Delta\mu/\mu$ in quasar absorbers is expected to be at the same level as in the interstellar clouds, i.e. $\sim 10^{-8}-10^{-7}$. This level of accuracy can be probed with the next generation of high resolution spectrographs such as ESPRESSO planned for the Very Large Telescope [81].

E. Temporal vs spatial variability of μ

Our measurements of $\Delta\mu/\mu$ being formally divided by the distance to the sources in light years imply a time variation of $\Delta\mu/\mu$ of about $10^{-11}-10^{-10}$ yr^{-1}. This variation rate is orders of magnitude larger than the laboratory bound quoted in Sect. I, $|\dot\mu/\mu| < 10^{-13}$ yr^{-1}, and than the extragalactic bounds based on the upper limit on $\Delta\mu/\mu$ at $z \sim 3$, $|\dot\mu/\mu| < 6\times10^{-16}$ yr^{-1} [18], and at $z = 0.68$, $|\dot\mu/\mu| < 4\times10^{-16}$ yr^{-1} [19]. Such glaring discrepancy may serve as another argument in favor of chameleon-type models: due to principal dependence of couplings and masses on matter density the laboratory bounds and astronomical measurements cannot be directly compared. Taken at face values, we may suggest that the rate of the spatial variations of μ exceeds significantly the rate of temporal variations.

V. CONCLUSIONS

In this paper we propose to use the ammonia inversion transitions in conjunction with low-lying rotational transitions of other molecules to probe the spatial changes of the electron-to-proton mass ratio μ from observations of molecular clouds located in the disk of the Milky Way at different galactocentric distances.

The reported estimates of $\Delta\mu/\mu$ are obtained for the Perseus molecular cores [34], the Pipe Nebula [65], and

the infrared dark clouds [36]. We found evidence for the spatial variability of μ at the level of $\Delta\mu/\mu \sim (4-14) \times 10^{-8}$ which is the most accurate astrophysical value to date. The statistical reliability of this result seems to be high enough but some instrument systematics could be possible. The revealed positive velocity offset between the NH_3 inversion transition and rotational transitions of other molecules should be confirmed by independent observations at different radio telescopes.

The result obtained can be compared with other tests of spatial variations of physical constants in the solar system which are based on atomic clock laboratory measurements. Thus, if $\Delta\mu/\mu$ follows the gradient of the local gravitational potential, as suggested in some scalar field models, then our estimate of $\Delta\mu/\mu$ contradicts significantly (~ 5 orders of magnitude) the atomic clock constraints obtained at different points in the gravitational potential of the Sun on the Earth's orbit. However, the measured signal of $\Delta\mu/\mu \sim (4-14)\times10^{-8}$ is in agreement with chameleon-type scalar field models which predict a strong dependence of masses and coupling constants on the ambient matter density.

To be completely confident that the derived velocity shift is not due to kinematic effects in the clouds but is the appearance of the spatial variation of $\Delta\mu/\mu$, new high precision radio-astronomical observations are needed for a wider range of objects. Such observations should include essentially optically thin lines of molecules co-spatially distributed with ammonia in order to reduce the Doppler noise. It is also desirable to increase the accuracy of the rest frequencies of the CCS $(2_1 - 1_0)$ and N_2H^+ $(1-0)$ transitions since their present uncertainties translate into the radial velocity error of ~ 13 m s^{-1} whereas the error of the velocity shift between, for instance, CCS and NH_3 in the Perseus cloud can be as small as 5 m s^{-1} (Table II).

In addition, the search for spatial variations of the fine-structure constant α in the Milky Way using mid- and far-infrared fine-structure transitions in atoms and ions [82], or the search for spatial variations of the combination of α^2/μ using the [C II] $\lambda158$ μm line and CO rotational lines [83] would be of great importance for cross-checking the results.

Acknowledgments

The authors are grateful to Eric Rosolowsky, Takeshi Sakai, and Jill Rathborne who sent us additional comments on their observations and data reduction. We thank Paola Caselli, Irina Agafonova, Keith Olive, and Thomas Dent for useful comments and discussions on the topic, and Alexander Lapinov for computed frequencies of the HC_3N $J = 5-4$ hyperfine transitions on which Table VII and Sect. IV A are based. This work is supported by the RFBR grants 06-02-16489, 07-02-00210, 08-02-00460, and by the Program 'Leading Scientific Schools of RF' (grant NSh-2600.2008.2).

[1] A. G. Riess, A. V. Filippenko, P. Challis, et al., Astron. J. **116**, 1009 (1998).
[2] A. G. Riess, R. P. Kirshner, B. P. Schmidt, et al., Astron. J. **117**, 707 (1999).
[3] S. Perlmutter, G. Aldering, G. Goldhater, et al., Astrophys. J. **517**, 565 (1999).
[4] E. J. Copeland, M. Sami, and S. Tsujikawa, Int. J. Mod. Phys. D **15**, 1753 (2006).
[5] R. R. Caldwell, R. Dave, and P. J. Steinhardt, Phys. Rev. Lett. **80**, 1582 (1998).
[6] P. J. E. Peebles, and B. Rata, Rev. Mod. Phys. **75**, 559 (2003).
[7] A. Balbi, C. Baccigalupi, F. Perrotta, and N. Vittorio, Astrophys. J. **547**, L89 (2001).
[8] V. V. Flambaum, and M. G. Kozlov, arXiv: physics.atom-ph/0711.4536 (2007).
[9] T. Rosenband, D. B. Hume, P. O. Schmidt, et al., Sciencexpress Report, 6 March, p. 1 (2008).
[10] M. T. Murphy, J. K. Webb, and V. V. Flambaum, Mon. Not. R. Astron. Soc. **384**, 1053 (2008).
[11] R. Srianand, H. Chand, P. Petitjean, and B. Aracil, Phys. Rev. Lett. **100**, 029902 (2008).
[12] P. Molaro, S. A. Levshakov, S. Monai, et al., Astron. Astrophys. **481**, 559 (2008).
[13] D. F. Mota, and J. D. Barrow, Mon. Not. R. Astron. Soc. **349**, 291 (2004).
[14] D. F. Mota, and J. D. Barrow, Phys. Lett. B **581**, 141 (2004).
[15] A. Shelkovnikov, R. J. Butcher, C. Chardonnet, and A. Amy-Klein, Phys. Rev. Lett. **100**, 150801 (2008).
[16] E. Reinhold, R. Buning, U. Hollenstein, et al., Phys. Rev. Lett. **96**, 151101 (2006).
[17] M. Wendt, and D. Reimers, arXiv: astro-ph/0802.1160 (2008).
[18] J. A. King, J. K. Webb, M. T. Murphy, and R. F. Carswell, arXiv: astro-ph/0807.4366 (2008).
[19] V. V. Flambaum, and M. G. Kozlov, Phys. Rev. Lett. **98**, 240801 (2007).
[20] J. D. Barrow, Phys. Rev. D **71**, 083520 (2005).
[21] J. D. Barrow, and J. Magueijo, Phys. Rev. D **72**, 043521 (2005).
[22] S. Blatt, A. D. Ludlow, G. K. Campbell, et al., Phys. Rev. Lett. **100**, 140801 (2008).
[23] S. J. Ferrell, A. Cingöz, A. Lapierre, et al., Phys. Rev. A **76**, 062104 (2007).
[24] J. Khoury, and A. Weltman, Phys. Rev. Lett. **93**, 171104 (2004).
[25] J. Khoury, and A. Weltman, Phys. Rev. D **69**, 044026 (2004).
[26] S. S. Gubser, and J. Khoury, Phys. Rev. D **70**, 104001 (2004).
[27] P. Brax, C. van de Bruck, A. C. Davis, J. Khoury, and A. Weltman, Phys. Rev. D **70**, 123518 (2004).
[28] B. Feldman, and A. E. Nelson, J. High Energy Phys. **08**,

002 (2006).
[29] A. Upadhye, S. S. Gubser, and J. Khoury, Phys. Rev. D **74**, 104024 (2006).
[30] K. A. Olive, and M. Pospelov, Phys. Rev. D **77**, 043524 (2008).
[31] A. S. Chou, W. Wester, A. Baumbaugh, et al., arXiv: hep-ex/0806.2438 (2008).
[32] J. van Veldhoven, J. Küpper, H. L. Bethlem, et al., Eur. Phys. J. D **31**, 337 (2004).
[33] D. R. Flower, G. Pineau des Forêts, and C. M. Walmsley, Astron. Astrophys. **456**, 215 (2006).
[34] E. W. Rosolowsky, J. E. Pineda, J. B. Foster, et al., Astrophys. J. Sup. **175**, 509 (2008).
[35] E. W. Rosolowsky (private communication).
[36] T. Sakai, N. Sakai, K. Kamegai, et al., Astrophys. J. **678**, 1049 (2008).
[37] T. Sakai (private communication).
[38] J. Di Francesco, N. J., II Evans, P. Caselli, et al., in *Protostars and Planets. V.*, edited by B. Reipurth, D. Jewitt, and K. Keil (Uni. Arizona Press, Tucson, 2007), p. 17 (arXiv: astro-ph/0602379)
[39] E. Keto, and P. Caselli, arXiv: astro-ph/0804.0822 (2008).
[40] P. T. P. Ho, and C. H. Townes, Ann. Rev. Astron. Astrophys. **21**, 239 (1983).
[41] P. J. Benson, and P. C. Myers, Astrophys. J. Sup. **71**, 89 (1989).
[42] P. Caselli, P. S. Meyers, and P. Thaddeus, Astrophys. J. **455**, L77 (1995).
[43] B. E. Turner, Astrophys. J. **449**, 635 (1995).
[44] M. Tafalla, P. S. Meyers, P. Caselli, and C. M. Walmsley, Astron. Astrophys. **416**, 191 (2004).
[45] P. Caselli, P. J. Benson, P. S. Meyers, and M. Tafalla, Astrophys. J. **572**, 238 (2002).
[46] S. Saito, K. Kawaguchi, S. Yamamoto, et al., Astrophys. J. **317**, L115 (1987).
[47] H. Suzuki, S. Yamamoto, M. Ohishi, et al., Astrophys. J. **392**, 551 (1992).
[48] Y. Hirahara, H. Suzuki, S. Yamamoto, et al., Astrophys. J. **394**, 539 (1992).
[49] T. B. H. Kuiper, W. H. Langer, and T. Velusamy, Astrophys. J. **468**, 761 (1996).
[50] S.-T. Lai, T. Velusamy, W. H. Langer, and T. B. H. Kuiper, Astron. J. **126**, 311 (2003).
[51] I. de Gregorio-Monsalvo, C. J. Chandler, J. F. Gómez, et al., Astrophys. J. **628**, 789 (2005).
[52] I. de Gregorio-Monsalvo, J. F. Gómez, O. Suárez, et al., Astrophys. J. **642**, 319 (2006).
[53] P. J. Benson, P. Caselli, and P. C. Myers, Astrophys. J. **506**, 743 (1998).
[54] W. J. Lafferty, and F. J. Lovas, J. Phys. Chem. Ref. Data **7**, 441 (1978).
[55] S. Yamamoto, S. Saito, K. Kawaguch, and M. Ohishi, Astrophys. J. **361**, 318 (1990).
[56] H.-H. Lee, E. Herbst, G. Pineau des Forêts, F. Roueff, and J. Le Bourlot, Astron. Astrophys. **311**, 690 (1996).
[57] J. A. Barranco, and A. A. Goodman, Astrophys. J. **504**, 207 (1998).
[58] J. Swift, W. J. Welch, and J. Di Francesco, Astrophys. J. **620**, 823 (2005).
[59] C. J. Lada, E. A. Bergin, J. F. Alves, and T. L. Huard, Astrophys. J. **586**, 286 (2003).
[60] A. J. Walsh, P. C. Myers, and M. G. Burton, Astrophys. J. **614**, 194 (2004).
[61] J. P. Williams, C. W. Lee, and P. C. Myers, Astrophys. J. **636**, 952 (2006).
[62] P. C. Myers, Astrophys. J. **270**, 105 (1983).
[63] C. F. McKee, and J. C. Tan, Astrophys. J. **585**, 850 (2003).
[64] F. R. Hampel, E. M. Ronchetti, P. J. Rousseeuw, and W. A. Stahel, *Robust Statistics. The Approach Based on Influence Functions* (John Wiley & Sons, New York, 1986).
[65] J. M. Rathborne, C. J. Lada, A. A. Muench, J. F. Alves, and M. Lombardi, Astrophys. J. Sup. **174**, 396 (2008).
[66] T. Pillai, F. Wyrowski, S. J. Carey, and K. M. Menten, Astron. Astrophys. **450**, 569 (2006).
[67] A. V. Lapinov, in *15th Symp. on High-Resolution Molecular Spectroscopy*, edited by Y. N. Ponomarev, S. N. Mikhailenko, and L. N. Sinitsa, Proceed. of SPIE, Vol. 6580, p. 658001 (2006).
[68] A. V. Lapinov (private communication).
[69] S. G. Kukolich, Phys. Rev. **156**, 83 (1967).
[70] H. S. P. Möller, S. Thorwirth, D. A. Roth, and G. Winnewisser, Astron. Astrophys. **370**, L49 (2001).
[71] H. S. P. Möller, F. Schlöder, J. Stutzki, and G. Winnewisser, J. Mol. Struct. **742**, 215 (2005).
[72] L. Lindegren, and D. Dravins, Astron. Astrophys. **410**, 1185 (2003).
[73] M. A. Gordon, in *Methods of Experimental Physics. XII.*, edited by M. L. Meeks (Academic, New York, 1976).
[74] J. D. Bekenstein, Phys. Rev. D **25**, 1527 (1982).
[75] V. V. Flambaum, Int. J. Mod. Phys. A **22**, 4937 (2007).
[76] V. V. Flambaum, and E. V. Shuryak, in *AIP Conf. Proceed.*, Vol. 995, p. 1 (2008).
[77] M. Miyamoto, and R. Nagai, Publ. Astron. Soc. Japan **27**, 533 (1975).
[78] M. Miyamoto, C. Satoh, and M. Ohashi, Astron. Astrophys. **90**, 215 (1980).
[79] H. Nishikori, M. Machida, and R. Matsumoto, Astrophys. J. **641**, 862 (2006).
[80] F. Eisenhauer, R. Schödel, and R. Genzel, Astrophys. J. **597**, L121 (2003).
[81] P. Molaro, arXiv: astro-ph/712.4390 (2007).
[82] M. G. Kozlov, S. G. Porsev, S. A. Levshakov, D. Reimers, and P. Molaro, Phys. Rev. A **77**, 032119 (2008).
[83] S. A. Levshakov, D. Reimers, M. G. Kozlov, S. G. Porsev, and P. Molaro, Astron. Astrophys. **479**, 719 (2008).